

1
2
3 **Stretching of the retinal pigment epithelium contributes to zebrafish optic cup**
4 **morphogenesis**
5

6
7 Tania Moreno-Mármol^{1,2}, Mario Ledesma-Terrón¹, Noemí Tabanera^{1,2}, María Jesús Martín-
8 Bermejo^{1,2}; Marcos J Cardozo^{1,2}, Florencia Cavodeassi^{1,2#} and Paola Bovolenta^{1,2*}
9

10 ¹ Centro de Biología Molecular Severo Ochoa, CSIC-UAM, c/ Nicolás Cabrera, 1, Campus de
11 la Universidad Autónoma de Madrid, Madrid 28049, Spain; ² CIBER de Enfermedades Raras
12 (CIBERER) Madrid 28049, Spain.
13
14
15

16 **Running title:** RPE and optic cup morphogenesis
17

18 **Key words:** actomyosin, squamous epithelium, microtubules, mechanical forces, proliferation
19

20 **# Present address:** St. George's, University of London, Cranmer Terrace, SW17 0RE,
21 London, UK
22

23 ***Corresponding author:** pbovolenta@cbm.csic.es
24
25
26
27

28 **Abstract**

29 The vertebrate eye-primordium consists of a pseudostratified neuroepithelium, the optic
30 vesicle (OV), in which cells acquire neural retina or retinal pigment epithelium (RPE) fates.
31 As these fates arise, the OV assumes a cup-shape, influenced by mechanical forces generated
32 within the neural retina. Whether the RPE passively adapts to retinal changes or actively
33 contributes to OV morphogenesis remains unexplored. We generated a zebrafish Tg(E1-
34 *bhlhe40*:GFP) line to track RPE morphogenesis and interrogate its participation in OV
35 folding. We show that, in virtual absence of proliferation, RPE cells stretch and flatten,
36 thereby matching the retinal curvature and promoting OV folding. Localized interference with
37 the RPE cytoskeleton disrupts tissue stretching and OV folding. Thus, extreme RPE flattening
38 and accelerated differentiation are efficient solutions adopted by fast-developing species to
39 enable timely optic cup formation. This mechanism differs in amniotes, in which proliferation
40 drives RPE expansion with a much-reduced need of cell flattening.

41

42 **Introduction**

43 The retinal pigment epithelium (RPE) is an essential component of the vertebrate eye,
44 composed of a monolayer of pigment-enriched epithelial cells abutting the neural retina (NR)
45 with a primary role in photoreception (1). Despite the acquisition of specialized epithelial
46 properties, RPE cells have a neural origin and share progenitors with the NR. These
47 progenitors are organized in a pseudostratified neuroepithelium, known as optic vesicle (OV)
48 or eye primordium. In amniotes, the OVs appear as balloon-like structures positioned at the
49 sides of the anterior neural tube (2). In zebrafish instead, these primordia are flat and form
50 two bi-layered structures with the outer and inner layers distally connected by a rim or hinge
51 (3). Under the influence of inductive signals (4,5), the two layers activate different genetic
52 programs that specify the cells of the inner layer and ventral outer layer as NR and those of
53 the dorsal outer layer as RPE (6–8). Whilst this specification occurs, the OV bends assuming
54 a cup-like shape (9).

55 The discovery of the *ojoplano* medaka fish mutant –affecting a transmembrane protein
56 localised at the basal end feet of NR cells (10)– in which the OV remains unfolded, was
57 instrumental to propose that basal constriction of NR progenitors is at the basis of OV
58 bending (10). This basal constriction is mediated by the redistribution of the actomyosin
59 cytoskeleton (10–12), which also enables the apical relaxation of retinal cells (13), enhanced
60 by focal adhesions of the apical surface with the extracellular matrix molecules (ECM) such
61 as laminin (12). The importance of concomitant apical relaxation, especially of the cells
62 positioned at the hinge, has been also supported in studies of mammalian retinal organoids
63 (14,15). Nevertheless and independently of their relative contribution, the acquisition of
64 apical convexity and basal concavity in the NR epithelium are accepted drivers of the
65 biomechanical forces that induce OV folding (15). In zebrafish, this mechanism is reinforced
66 by rim involution or epithelial flow, a process whereby progenitors at the hinge emit dynamic
67 lamellipodia at the basal side and actively translocate from the ventral outer layer of the OV
68 into the inner/retinal layer (3,13,16–19). Periocular neural crest cells appear to facilitate this
69 flow, in part by the deposition of the ECM (20) to which the lamellipodia attach (13,17,18).
70 The result of this flow is an unbalanced cell number between the two layers, which should
71 favour NR bending (13,17,18). Whether this flow may also contribute to the concomitant cell
72 shape modifications that the remaining outer layer cells undergo as they become specified
73 into RPE, or conversely whether RPE specification favours the flow (17), remain open
74 questions.

75 Indeed as the OV folds, the pseudostratified neuroepithelial cells of the OV dorsal
76 outer layer progressively align their nuclei becoming a cuboidal monolayer in amniotes
77 species (2,21). In zebrafish, cuboidal cells further differentiate to a flat/squamous epithelium
78 (16,18) that spreads to cover the whole apical surface of the NR (16,22). In mice, failure of
79 RPE specification, as observed after genetic inactivation of key specifier genes (i.e.
80 *Otx1/Otx2*, *Mitf*, *Yap/Taz*), enables RPE progenitors to acquire a NR fate (23–25). The
81 resulting optic cups (OCs) present evident folding defects (23), raising the possibility that
82 specific RPE features are needed for OC formation. In line with this idea, a differential
83 stiffness of the RPE versus the NR layer has been proposed to drive the self-organization of
84 mammalian organoids into an OC (14,15,26). Furthermore, generation of proper RPE cell
85 numbers seems a requirement for correct OC folding in mice (27). However, studies
86 addressing the specific contribution of the RPE to OV folding are currently lacking.

87 Here we report the generation of a Tg(E1-*bhlhe40*:GFP) zebrafish transgenic line with
88 which we followed the beginning of RPE morphogenesis under both normal and interfered
89 conditions. We show that, whereas in amniotes, including humans, the developing RPE
90 undergo proliferation to increase its surface with a less evident cell flattening, zebrafish RPE
91 cells rapidly cease proliferation and expand their surface by reducing their length along the
92 apico-basal axis and extending in the medio-lateral direction with a tissue-autonomous
93 process that depends on cytoskeletal reorganization. Localized interference with either the
94 retinal or the RPE actomyosin and microtubule cytoskeleton shows that RPE flattening
95 generates a mechanical force that actively contributes to OV folding, complementing the force
96 generated by the basal constriction of the NR. This mechanism represents an efficient solution
97 to match the increased apical surface of the NR layer in a fast-developing vertebrate species
98 such as zebrafish.

99

100 **Results**

101 ***Generation of a specific reporter line to study zebrafish RPE development***

102 Detailed analysis of zebrafish RPE morphogenesis has been hampered by the lack of a
103 suitable transgenic line, in which RPE cells could be followed from their initial commitment.
104 The E40 (*bhlhe40*) gene, a basic helix-loop-helix family member, encodes a light and
105 hypoxia-induced transcription factor (also known as *Dec1*, *Stra13*, *Sharp2* or *Bhlhb2*)
106 involved in cell proliferation and differentiation as well as in the control of circadian rhythms
107 (28). In neurulating zebrafish embryos, its expression is limited to cells of the prospective
108 RPE (Fig. 1A) (22,29), representing a potentially suitable tissue marker.

109 We used predictive enhancer and promoter epigenetic marks at different zebrafish
110 developmental stages (30) to scan the *bhlhe40* locus for the presence of conserved and active
111 regulatory regions. The promoter and four potential enhancers (E1-4; Fig. 1B) appeared to be
112 active between 80% epiboly and 24 hpf, encompassing the early stages of zebrafish eye
113 development (30). These enhancers were selected, amplified and tested using the ZED vector
114 (31) as potential drivers of gene expression in the prospective RPE. The resulting F0 embryos
115 were raised to adulthood and screened. Only the E1 enhancer drove specific and restricted
116 GFP reporter expression into the prospective RPE. The corresponding fishes were further
117 crossed to establish the stable transgenic line Tg(E1-*bhlhe40*:GFP) used in this study.

118 Time-lapse studies of the Tg(E1-*bhlhe40*:GFP) progeny confirmed that the transgenic
119 line faithfully recapitulated the *bhlhe40* mRNA expression profile detected with *in situ*
120 hybridization (Fig. 1A,C). GFP reporter expression appeared in a discrete group of
121 neuroepithelial cells in the dorso-medial region of the OV (16-17 hpf) and expanded both
122 posteriorly and ventrally (Fig. 1C; Video 1 and 2), so that, by 24 hpf, GFP positive cells
123 appeared to wrap around the entire inner NR layer. 3D reconstructions of selected embryos
124 further confirmed the fast (about seven hours) expansion of the GFP-positive domain forming
125 an outer shell for the eye (Fig. 1D). Apart from a faint and very transient signal in some early
126 NR progenitors — likely due to the existence of negative regulatory elements not included in
127 the construct — no GFP expression was observed in regions other than the RPE during this
128 process. However, after the formation of the OC, reporter expression appeared also in the
129 ciliary marginal zone (CMZ), the pineal gland and few neural crest cells surrounding the eye
130 (Fig. 1C; Video 1-3). These additional domains of expression coincided with the reported
131 *bhlhe40* mRNA distribution (29) and represented no obstacle for using the transgenic line as a
132 tool to follow the early phases of RPE generation. Indeed, very early activation represents an

133 important advantage of the Tg(E1-*bhlhe40*:GFP) line over other presently available transgenic
134 lines that allow visualizing the RPE (32,33).

135 The suitability of the Tg(E1-*bhlhe40*:GFP) line for the identification of the very first
136 RPE cells is supported by the onset of the reporter expression in the dorso-medial OV region,
137 coinciding with previous fate map predictions (16,18). To further verify this notion, we took
138 advantage of the characteristic of the fluorescent Kaede protein (34) that switches from green
139 to red emission upon UV illumination. Embryos were injected with Kaede mRNA and
140 neuroepithelial cells located at the most dorso-medial region of the OV were UV illuminated
141 at the 15 hpf stage to ensure that no differentiation had yet occurred (Fig. 1E). Embryos were
142 let develop until 30 hpf. Photoconverted cells were found throughout the thin outer layer of
143 the OC (Fig. 1E), confirming that the entire RPE derives from the dorso-medial OV region.

144 ***Neuroepithelial cell flattening drives RPE expansion at OV stages***

145 Tg(E1-*bhlhe40*:GFP) embryos were thereafter used to dissect the extensive changes in cell
146 shape that are associated with the acquisition of RPE identity (16,22). At OV stage all retinal
147 progenitors present a columnar-like morphology characteristic of embryonic neuroepithelia
148 (Fig. 2A,A'). As soon as RPE progenitors begin to express the transgenic GFP reporter, their
149 apico-basal length rapidly and progressively reduces (Fig. 2A-C'), so that the cells first
150 assume a cuboidal shape (Fig. 2B,B') and then become flat, forming a squamous epithelial
151 monolayer overlaying the apical surface of the NR (Fig. 2C,C'). At 30 hpf, RPE cells
152 presented a polygonal, frequently hexagonal, morphology (Fig. 2D,D'), with an apical surface
153 area that, on average became about eightfold larger than that observed in progenitor (PN) cells
154 (Fig. 2F; RPE \bar{a} : $354.8 \pm 100.3 \mu\text{m}^2$ vs PN \bar{a} : $43.7 \pm 7.8 \mu\text{m}^2$). In contrast, the abutting apical
155 surface of NR cells slightly shrank as compared to that of PN cells (Fig. 2E,E',F; NR \bar{a} : 22.5
156 $\pm 2.9 \mu\text{m}^2$ vs PN \bar{a} : $43.7 \pm 7.8 \mu\text{m}^2$) while maintaining a constant apico-basal length. The
157 latter observation agrees with previous reports showing that the cone-like morphology of NR
158 progenitors represents only a slight modification of the progenitor columnar shape (11,13).

159 To obtain a quantitative analysis of the dynamic changes that RPE tissue, as whole,
160 underwent during OV folding, we performed a morphometric characterization of the images
161 from Videos 1-3. To this end, the fluorescent information from the Tg(E1-*bhlhe40*:GFP)
162 reporter was discretized into seven different segments that were individually analysed along
163 the recording time (Fig. 3-figure supplement 1; material and methods). The combined
164 quantification of the different segments (Fig. 3A; Fig. 3-figure supplement 1) showed that,
165 between stages 17 and 21 hpf, the overall thickness of the RPE tissue underwent, on average,

166 a flattening of more than threefold (from a mean of about 24 to 8 μm ; Fig. 3B). Flattening
167 occurred with a central to peripheral direction, so that RPE cells closer to the hinges were the
168 last ones to flatten (Fig. 2C,C'). In parallel, the overall RPE surface underwent a \sim two-fold
169 expansion between 17 and 22 hpf (from approx. 1.1 to $2.2 \times 10^3 \mu\text{m}^2$; Fig. 3C; Videos 1-2),
170 reflecting the large increase in the apical area observed in each individual cell at later stages
171 (Fig. 2F). In line with the idea that cell flattening is *per se* sufficient to account for whole
172 tissue enlargement, the RPE volume only slightly changed between 17 and 20 hpf with a
173 slope increase of $0.47 \times 10^3 \mu\text{m}^3/\text{h}$ (Fig. 3D).

174 To provide further support to this idea we analysed the RPE volume variation in
175 comparison with the growth of the entire OC in two time windows: from 17 to 22 hpf (Videos
176 1-3) and from 24 to 37 hpf (Video 4), using GFP (RPE) and RFP (eye) reporter signals from
177 the double Tg(E1-*bhlhe40*:GFP; *rx3*:GAL4;UAS;RFP) line or from the Tg(E1-*bhlhe40*:GFP)
178 line injected with the pCS2:*H2B-RFP* mRNA (Fig. 3E,F). Signal quantification showed that
179 the eye underwent a marked and linear volume increase (slope: $5.54 \times 10^4 \mu\text{m}^3/\text{h}$ from 17 to
180 22 hpf and $3.6 \times 10^4 \mu\text{m}^3/\text{h}$ from 24 to 37 hpf) as compared to that of the RPE (Fig. 3D,G).
181 Between 20 and 22 hpf the reporter starts being expressed in the posterior and, to a lesser
182 extent, in the anterior CMZ (GFP-CMZ domain, Video 1-2). Consistently with the onset of
183 GFP-CMZ expression, RPE reporter volume suddenly expanded between 20 and 22 hpf
184 (slope: $1.25 \times 10^4 \mu\text{m}^3/\text{h}$; Fig. 3G) to then slow back between 24 to 37 hpf (slope: 1.2×10^3
185 $\mu\text{m}^3/\text{h}$; Fig. 3G). Confirming this association, only the tissue segments very close to the
186 posterior CMZ had a volume larger than that of the RPE at 17-20 hpf (Fig. 3-figure
187 supplement 1), whereas the GFP-positive RPE domain located in the most central regions
188 presented a volume undistinguishable from that detected at previous stages. In sum, a
189 comparison of the dynamics slopes from the GFP-RPE domain and OV regions suggests that
190 the volume of the RPE grows at very low pace ($0.47 \times 10^3 \mu\text{m}^3/\text{h}$) – despite the rather drastic
191 morphological changes of its cells –, whereas the whole OV expands at a pace \sim twenty-five
192 times faster ($1.25 \times 10^4 \mu\text{m}^3/\text{h}$; Fig. 3D)

193 Taken all together, this morphometric analysis indicates that the expansion of the RPE
194 in zebrafish occurs by recruiting a limited number of cells that undergo profound cell shape
195 changes: from a neuroepithelial to squamous morphology.

196

197 ***RPE flattening is a tissue autonomous process required for proper OV folding***

198 Both external interactions and intracellular processes determine the shape of a cell and define
199 its mechanical properties (35). Thus, in principle, RPE flattening might occur as a “passive”

200 process, triggered by the forces that the NR and hinge cells exert on the RPE (2,17).
201 Alternatively, it might depend on cell or tissue autonomous cytoskeletal rearrangements,
202 involving, for example, myosin II activity, which controls the acquisition of a flat epithelial
203 morphology in other contexts (36,37). Discriminating between these two possibilities has
204 been technically difficult. Experiments directed to assess the mechanisms of OV folding have
205 used whole embryo bathing in drugs such as blebbistatin (11,13), a specific myosin II
206 inhibitor (38). Such an approach hampers the assessment of the potential influence of NR
207 over RPE morphogenesis (and vice-versa) as well as the relative contribution of the two
208 tissues to OV folding. We sought to overcome this limitation by spatially localized
209 interference with the cytoskeletal organization of either the RPE or NR and by recording the
210 tissue autonomous and non-autonomous consequences. Nevertheless, to begin with, we
211 reproduced the whole embryo bathing approach used by others (11,13), focusing on the yet
212 unreported effect that blebbistatin had on the RPE.

213 Tg(E1-*bhlhe40*:GFP) embryos were bathed either in blebbistatin or its diluent
214 (DMSO) at 17 hpf (the onset of RPE specification; Fig. 4A-C) and then let develop up to 19.5
215 hpf, when embryos were analysed. DMSO-treated (control) embryos developed normally
216 forming an OC surrounded by a squamous RPE (Fig. 4B). In blebbistatin-treated embryos,
217 NR cells did not undergo basal constriction and the OV remained unfolded (Fig. 4C), as
218 previously described (11,13). Notably, in almost all the embryos analysed (n=44/49) RPE
219 cells did not flatten but remained cuboidal in shape (Fig. 4C). A similar phenotype was
220 observed after treatment with para-nitro-blebbistatin, a non-cytotoxic and photostable version
221 of blebbistatin (Fig. 4D). These observations support that lack of OV folding is associated
222 with alterations in both the retina and RPE. To uncouple the two events, we turned to the
223 photoactivable compound azido-blebbistatin (Ableb), which binds covalently to myosin II
224 upon two-photon irradiation, thus permanently interfering with myosin II activity in a
225 spatially restricted manner, as already proven (39,40). Tg(E1-*bhlhe40*:GFP) 17 hpf embryos
226 were bathed in Ableb or in DMSO and irradiated in a small region of either the dorsal outer
227 layer (RPE) or the inner retinal layer (retina) of the OV (see methods). Embryos were then let
228 develop until 24 hpf. During this period, the irradiated RPE cells underwent anterior and
229 medio-lateral spreading — likely coinciding with the reported pinwheel “movement” (18) —
230 and were mostly found in the ventral half of the OV. Notably, Ableb photoactivation in the
231 prospective RPE cells reproduced, although slightly less efficiently (n=30/44 embryos), the
232 phenotype observed upon whole embryo bathing in blebbistatin, in which RPE cells acquired
233 a cuboidal morphology (Fig. 4C,D,G,G’). No detectable alterations were found in the OV of

234 irradiated/DMSO treated embryos or in the contralateral non-irradiated OV of embryos
235 incubated in Ableb regardless of the irradiated region (Fig. 4E-F', H-I'). Cell shape
236 quantifications showed a significantly longer apico-basal axis (Fig. 4E'-G') in irradiated
237 Ableb RPE cells, normalized to that of control (DMSO and Ableb treated non-irradiated) OVs
238 (Fig. 4K; Mann-Whitney U test, $z=-5.088$, $p<0.001$, control mean length 15.96 vs Ableb-
239 treated 38.03). Failure of cell flattening in the irradiated region of the RPE was consistently
240 associated with a significant reduction of OV folding (Fig. 4E-G), as assessed by measuring
241 the invagination angle (13), which was normalized to that of control embryos (Fig. 4L; Mann-
242 Whitney U test: $z=-2.704$, $p<0.01$, mean rank for control 21.60 vs Ableb-treated 33.33).
243 Photo-activation of Ableb in similar areas of the prospective NR basal region resulted in an
244 elongated NR and a significantly impaired OV folding (Fig. 4J), as determined by the
245 invagination angles normalized to those of control OV (Fig. 4N; Mann-Whitney U test: $z=-$
246 3.035 , $p<0.01$, mean rank control 10.29 vs Ableb 20.06). Notably, disruption of NR
247 morphogenesis had no consequences on RPE development in all the analysed embryos
248 ($n=16/22$): cells underwent normal flattening with apico-basal lengths comparable to those of
249 controls (Fig. 4H'-J', M; Mann-Whitney U test: $z=0.582$, $p>0.05$, mean rank control 14.50 vs
250 Ableb 16.38). These data strongly support that RPE flattening is not secondary to NR folding
251 but rather a tissue autonomous event. They also indicate that OV folding requires forces
252 independently generated in both the NR and RPE. Notably, blebbistatin or Ableb treatments
253 did not compromise the expression of the Tg(E1-*bhlhe40*:GFP) transgene in any experimental
254 condition, indicating that cellular tension and morphology did not affect RPE specification.

255 Microtubule dynamics has an important role in determining the shape of a cell (41). For
256 example, reorientation of the microtubule cytoskeleton from the apico-basal to the medio-
257 lateral cell axis together with actin filaments redistribution seems to drive the conversion of
258 the *Drosophila* amnioserosa cells from a columnar to squamous epithelium (42). To
259 determine if a similar reorientation occurs in the RPE, we used time-lapse analysis of Tg(E1-
260 *bhlhe40*:GFP) embryos injected with the mRNA of EB3:GFP, a protein that binds to the plus
261 end of growing microtubules (43). In neuroepithelial RPE progenitors, microtubules grew in
262 the apico-basal direction, whereas growth turned to the medio-lateral plane, as the RPE cells
263 became squamous (Fig. 5-figure supplement 1; Video 5). To determine if this reorientation is
264 important for cell flattening, we bathed Tg(E1-*bhlhe40*:GFP) embryos in nocodazole, a drug
265 that interferes with microtubule polymerization, or its vehicle (DMSO) at either 16 or 17 hpf
266 (Fig. 5A,D) and then analysed them at 18.5 or 19.5 hpf, respectively. The eye of DMSO
267 treated embryos developed normally (Fig. 5B,E), whereas in the presence of nocodazole RPE

268 cells retained a columnar-like morphology with a stronger phenotype in embryos exposed to
269 the drug at an earlier stage (Fig. 5C). Nocodazole treatment did not prevent the activation of
270 the GFP reporter expression (Fig. 5C) or the acquisition/distribution of expected specification
271 (*otx1* and *mitf*) and apico-basal polarity (*zo-1* and laminin) markers (Fig. 5-figure supplement
272 2). Notably, although the NR layer appeared to bend inward, the RPE layer remained
273 unfolded (Fig. 5F) and outer layer cells accumulated at the hinge, suggesting a defect in rim
274 involution. This defect may be due to the alteration of microtubule polymerization in rim
275 cells. Alternatively, the lack of RPE stretching may prevent the translocation of rim cells to
276 the NR layer.

277 The whole embryo treatments described above did not allow us to determine the
278 differential requirement of microtubule dynamics in the RPE and the adjacent NR layer.
279 However, we were unable to uncouple the effect of microtubule alterations in the two OV
280 layers with localized drug interference. We thus resorted to use stathmin 1 (*STMNI*), a key
281 regulator of microtubule depolymerization (44). We generated a bidirectional UAS construct
282 (UAS:*STMNI*) driving the simultaneous production of GFP and *STMNI* under the same
283 regulatory sequences (45,46), which we injected in Tg(*rx3*:GAL4) embryos. We reasoned
284 that, although *rx3* drives transgene expression in both NR and RPE progenitors, the random
285 and sparse expression that occurs in F0 would be sufficient to separate the effect in the two
286 tissues. RPE cells expressing *STMNI* – and notably also those nearby – retained a cuboidal-
287 like shape with an abnormally increased apico-basal axis as compared to GFP-positive cells in
288 control UAS:GFP injected embryos. Even though cells in the inner OV layer appeared to still
289 undergo basal constriction (Fig. 5G-I), the OV as a whole underwent poor invagination (Fig.
290 5J).

291 All in all, the data derived from the manipulation of the actomyosin and microtubule
292 cytoskeleton suggest that the RPE actively participates in OV folding by undergoing a tissue
293 autonomous stretching driven by cell cytoskeletal rearrangements.

294

295 ***Differential requirement of cell proliferation in zebrafish vs amniotes RPE development***

296 Our finding that the zebrafish RPE largely grows through autonomous cell flattening agrees
297 with the observation that zebrafish RPE cells barely proliferate during OV folding (22).
298 Furthermore, pharmacological treatment of embryos to block cell division during OV folding
299 has little or no consequences on RPE expansion (22). These observations however differ from
300 reports in mouse embryos, in which RPE proliferation seems a requirement for OV folding
301 (27) and suggest the existence of species-specific modes of early RPE growth. We

302 hypothesized that these modes may be related to the speed of embryonic development with
303 final consequences on the epithelial characteristic of the RPE. To test this possibility, we
304 compared proliferation rate and apico-basal length of the zebrafish RPE (Fig. 6) with those of
305 the medaka, chick, mouse and human embryos at equivalent OV/OC stages (Fig. 7). In these
306 species, Otx2 and N-cadherin immunostaining was used to identify the RPE domain (23,47)
307 and the cell shape (Figure 7-figure supplement 1) respectively.

308 BrdU incorporation in Tg(E1-*bhlhe40*:GFP) embryos from early OV (17 hpf) to late
309 OC stages (48 hpf) showed a marked reduction of cell proliferation in the OV outer layer
310 (Fig. 6A-B), very much in line with the report that only 2% of the outer layer cells undergo
311 mitosis during this period (22). At the earlier stage (17 hpf), BrdU positive cells were
312 scattered across the RPE with no easily identifiable geometry and accounted for 49% of the
313 total RPE cells. This fraction dropped to about 20% at 19 hpf, when cells are flat, and then to
314 12% at 48 hpf (Fig. 6B) when the epithelium is maturing. Statistical analysis showed
315 significant differences between 17 and 20 hpf (Mann-Whitney U test: $z=-2.619$, $p<0.01$, mean
316 rank for 17 hpf is 8 and for 19 hpf is 3) and a clear correlation between proliferation rate and
317 developmental stage (Kruskal-Wallis test: $\chi^2(df=7, n=40)=32,023$; $p<0.001$). During this
318 period, the apico-basal axis of individual RPE cells flattened reaching a length of 3 μm at 22-
319 23 hpf. Thus, acquisition of RPE identity, cell shape changes and OV folding are associated
320 with a progressive reduction of cell proliferation in the OV outer layer.

321 OC morphogenesis in the teleost medaka fish occurs with a choreography comparable to
322 that of the zebrafish (17,18) but the medaka fish RPE does not adopt an extreme squamous
323 morphology (Fig 7A). Notably, medaka fish develop slower than zebrafish embryos, so that,
324 from first appearance, their OVs take about eight hours more to reach a fully developed OC
325 (26 vs 18 hr) (49), a time compatible with an additional round of cell division. Consistent with
326 this idea, BrdU incorporation in st18 to 22-23 medaka embryos showed that about 70% of the
327 cells in the OV outer layer were actively cycling and this proportion dropped to about 48% at
328 OC stage (Fig. 7A,E) with a slightly less evident decrease of the average apico-basal axis
329 (st18: 21.3 μm vs st23 3.5 μm ; Fig. 7A) as compared to the changes observed in zebrafish. An
330 equivalent analysis in chick and mouse embryos showed similar results. In these species OV
331 conversion into an OC takes about 27 and 48 hr, respectively. During this period a similar and
332 almost constant proportion of RPE progenitors incorporated BrdU (Fig. 7B,C,E), including
333 when cells acquired the expression of the RPE differentiation marker Otx2 (Figure 7-figure
334 supplement 1). Furthermore, RPE cells only roughly halved their apico-basal axis (chick:
335 HH12: 30.1 μm vs HH18: 15.8 μm ; mouse: E9.5: 23.7 μm vs E11.5 13 μm Fig. 7B,C),

336 suggesting that in slower developing species, proliferation but not stretching accounts for
337 RPE surface increase. To corroborate this idea, we next analysed human embryos.

338 The human eye primordium is first visible at about four-five weeks of gestation
339 corresponding to Carnegie stage (CS)13 (50). A fully formed OC is reached only roughly 10
340 days after, at CS16 (50). Immunostaining of paraffin sections from CS13 to CS16 embryos
341 with antibodies against Ki67, a marker of the active phases of the cell cycle, demonstrated
342 that the large majority of prospective RPE cells undergo a marked proliferation during the
343 transition from OV to OC (Fig. 7D). Owing to the difficulties in obtaining early human
344 embryonic samples, the percentage of proliferating cells could only be estimated, showing
345 that in the OTX2-positive domain (Fig. S4B), Ki67-positive RPE cells represented about 85%
346 to 75% of the total between CS13 and 16. During this period, the prospective RPE layer
347 always appeared as a rather thick pseudostratified epithelium with an organization resembling
348 that of the NR composed of densely packed and elongated neuroepithelial cells (Fig. 7D;
349 Figure 7-figure supplement 1). During the formation of the OC, the RPE neuroepithelium
350 only slightly flattened (apico-basal thickness: CS13: 45 μ m vs CS16: 33.6 μ m), far from
351 reaching the cuboidal appearance seen at postnatal ages (Figure 7-figure supplement 1).

352 Collectively these data indicate that, in the absence of sufficient time for cell
353 proliferation, flattening is an efficient solution adopted by zebrafish RPE cells to enlarge the
354 whole tissue to the extent needed for OV folding. In other vertebrates, in which slower
355 development allows for more rounds of cell division, the RPE grows in a conventional
356 proliferation-based mode that correlates with a less evident flattening of RPE cells (Fig. 7F).

357

358 Discussion

359 The cup-shape of the vertebrate eye is thought to optimize vision (51). This shape is acquired
360 very early in development as the result of specification and morphogenetic events, during
361 which the NR and the RPE arise. Studies in teleosts (zebrafish and medaka) together with
362 mammalian organoid cultures have recently demonstrated a fundamental contribution of NR
363 progenitors in driving the acquisition of this cup shape (2,9). The role of the RPE progenitors
364 in this process has instead not been properly clarified. In this study, we have filled this gap
365 and analysed the folding of the zebrafish OV from the RPE perspective. This analysis has
366 been possible thanks to the generation of a new RPE reporter line (Tg(E1-*bhlhe40*:GFP), in
367 which GFP expression appears in the domain fated to originate the RPE. Following the cells
368 arising from this domain, we show that RPE surface expansion is an active and tissue
369 autonomous process required for OV folding. This expansion largely occurs by extreme cell
370 flattening with little contribution of cell proliferation, a mechanism that sets zebrafish RPE
371 morphogenesis apart from that of other analysed vertebrate species, in which proliferation
372 accounts for RPE growth.

373 Our analysis together with a previous report (22) shows that the onset *bhlhe40*
374 expression coincides spatially and temporally with that of zebrafish RPE specification. Thus,
375 the Tg(E1-*bhlhe40*:GFP) line serves as an early tissue specific marker that even precedes the
376 appearance of previously accepted *Otx* or *Mitf* tissue specifiers, as confirmed in a parallel
377 transcriptomic analysis (8). *Bhlhe40* expression in the RPE is conserved at least in mouse and
378 humans (8,52,53), suggesting a possible relevant function in this tissue. However, its
379 CRISP/Cas9 inactivation, alone or in conjunction with that of the related *bhlhe41*, *mitfa* and
380 *mitfb*, had no evident consequences on zebrafish RPE development, at least in our hands (data
381 not shown). One possible reason for the absence of an evident RPE phenotype is functional
382 redundancy with other untested members of the large family of the BHLH transcription
383 factors or that the gene has only later functions as reported (54). However, we favour the
384 alternative possibility that zebrafish RPE specification does not occur stepwise as in other
385 species (21,55) but “en bloc” with an almost simultaneous activation of all differentiation
386 genes. This would make the inactivation of one or two genes insufficient to perturb fate
387 acquisition. Such a mechanism is expected to provide robustness to a process that takes place
388 in just few hours and finds support in present and past findings (8,22).

389 Indeed, we and others (22) have shown that, by the time the OV starts to bend, the
390 large majority of RPE cells have already left the cell cycle and have acquired a differentiated

391 squamous morphology by undergoing a marked surface enlargement in the medio-lateral
392 direction and a reduction of the apico-basal axis. The net result is an overall modest volume
393 increase. Furthermore, blocking cell division as the OC forms does not interfere with RPE
394 expansion (22), strongly supporting a primary role of cell stretching in RPE expansion.
395 Consistently, transcriptomic analysis shows that during this same lag of time, RPE cells
396 repress genes characteristic of 16 hpf OV progenitors, such as *vsx1*, and acquire the
397 expression of RPE specific genes. These includes blocks of transcription factors, such as
398 known RPE specifiers (i.e. *otx*, *mitf*) and regulators of epidermal specification (i.e. *tfap* family
399 members, known regulator of keratin gene expression (56)) as well as several cytoskeletal
400 components, most prominently a large number of keratins and other desmosomal components
401 found in squamous epithelia (8). Thus, in just few hours (from 16 to 18 hpf) RPE cells acquire
402 the molecular machinery required for their conversion from a neuroepithelial to a squamous
403 and likely highly coupled epithelium. Our study shows that this conversion relays on a tissue
404 autonomous cytoskeletal reorganization without the influence of the morphogenetic events
405 occurring in the nearby NR. Indeed, local interference with actomyosin or microtubule
406 dynamics is sufficient to retain RPE cells into a cuboidal or neuroepithelial configuration,
407 respectively, without affecting their specification. In contrast, localized interference with NR
408 bending has no effect on RPE flattening. Notably, our studies also suggest that the RPE acts
409 in a “syncytial-like” manner, as mosaic interference with microtubule polymerization seems
410 to impact in the shape of the adjacent cells if not on the entire tissue. This is perhaps not
411 surprising given that mature RPE cells have been reported to be chemically coupled (57,58).
412 Furthermore, the presumptive RPE of the chick (unpublished observations) and zebrafish (8)
413 expresses high levels of connexion proteins (i.e. Gap-43), which are responsible for the
414 “syncytial-like” behaviour observed in brain astrocytes (59). This together with the additional
415 observation that st18 RPE cells express many desmosomal proteins (8) indicate that the tissue
416 becomes tightly connected very soon, perhaps behaving as a community (60).

417 The extreme flattening of the zebrafish RPE cells makes the resolution of their
418 cytoskeletal components difficult with *in vivo* confocal microscopy, hampering the complete
419 understanding of how the actomyosin cytoskeleton promotes the acquisition of a squamous
420 configuration. In other contexts, a flat morphology is associated with the presence of acto-
421 myosin stress fibres that compress the nucleus (36,37). Myosin II is essential for this
422 compressive role and its inhibition with blebbistatin causes the loss of the flat morphology
423 (36,37), as we have observed in blebbistatin and Ableb treated embryos. It is thus possible
424 that a similar nuclear compression may occur in the RPE cells as they flatten, although we

425 were unable to detect stress fibres around the nucleus, likely due to plasma membrane
426 proximity. Remodelling of the microtubular cytoskeleton seems to aid further RPE cell
427 flattening. Microtubules change their orientation during RPE morphogenesis, from being
428 aligned along the apico-basal axis of the cells at the onset of RPE morphogenesis, to
429 becoming aligned with the planar axis in squamous RPE cells. A similar process has been
430 described during the morphogenesis of the *Drosophila* amnioserosa (42), in which cells also
431 change from a columnar to a squamous morphology. In these cells, actin accumulation at the
432 apical edge seems to provide resistance to the elongation of microtubules, which thus bend,
433 leading to a 90° rotation of all subcellular components. This rotation is accompanied by a
434 myosin-dependent remodelling of the adherens junctions (42), a process that may also take
435 place during RPE flattening.

436 Although additional studies are needed to clarify the precise dynamics of the
437 cytoskeletal reorganization underlying RPE differentiation, our study demonstrates that
438 cytoskeletal dynamics occurs in a tissue autonomous manner. In contrast to other studies
439 (11,13), we have used a photoactivable version of blebbistatin that has allowed us to
440 determine the individual contribution of the NR and RPE to OV folding. As a drawback, this
441 approach allows to activate the drug only in relatively small patches of tissue. It was thus
442 rather remarkable to observe that failure of RPE flattening in small regions was sufficient to
443 decrease OV folding. This suggests that RPE stretching represents an additional and relevant
444 mechanical force that, together with retinal basal constriction and rim involution, contributes
445 to zebrafish eye morphogenesis (Fig. 8A). This flattening and stretching together with a
446 substantial expression of keratins (8) may confer a particular mechanical strength to the
447 zebrafish RPE, which, in turn, may constrain the NR at the same time favouring rim
448 involution (17). The latter possibility is supported by the observation that inner layer cells
449 seem to accumulate at the hinge in the absence of RPE flattening. Alternatively, this
450 accumulation may simply reflect that rim cell involution depends of intrinsic microtubule
451 polymerization, although previous studies have discarded this possibility (13). These marked
452 morphogenetic rearrangements can thus be seen as an efficient solution adopted in fast
453 developing species to make eye morphogenesis feasible in a period that does not allow for
454 proliferation-based tissue growth.

455 The perhaps obvious question is whether similar morphogenetic rearrangements are
456 needed in other vertebrates to form the remarkably conserved cup shape of the eye. So far,
457 rim involution has been reported only in teleost species where it may represent a fast mode of
458 increasing the surface of the inner layer of the OV, thus favouring its bending (13,17,18). This

459 idea is well in agreement with previous data showing that between 16 to 27 hpf the number of
460 cells in the outer layer of the OV decreases from about 587 to 432, whereas that of the inner
461 layer increases in a way that cannot be explained solely by proliferation (16). In other species,
462 this cell displacement may not be needed as the layer can grow by cell division. In a similar
463 way, we have shown here that in slower developing species, RPE cells maintain a higher
464 proliferation rate that contributes substantially to the increase of RPE surface while
465 undergoing less marked changes in cell shape (Fig. 8B). This correlation is visible in medaka,
466 despite its relative evolutionary proximity to zebrafish (49), and is maximal in human
467 embryos. Indeed, in humans, the RPE layer is composed of cells with a neuroepithelial
468 appearance and a high proliferation rate, despite the expression of OTX2, considered a tissue
469 specifier. Thus, in mammals, full commitment of the OV outer layer to an RPE identity may
470 occur over a prolonged period of time and not “en bloc” as in zebrafish, as suggested by
471 comparing RNA-seq data of RPE cells from human CS13-16 embryos (53) with those from
472 equivalent stages in zebrafish (8). Human RPE cells from CS13-16 embryos are still enriched
473 in the expression of proliferation associated genes (53) but not of those typical of squamous
474 epithelia as in zebrafish (8). A slow acquisition of RPE identity may also explain why, in
475 mice, inactivation of genes such as *Otx2*, *Mitf* or *Yap* causes the RPE layer to adopt NR
476 characteristic (23,25,61), whereas this feature that has never been reported after equivalent
477 manipulations in zebrafish (62,63), or why FGF8 can push the amniote but not the zebrafish
478 RPE layer to acquire a NR identity (64). As a reflection of this slower differentiation in
479 amniotes, RPE cells can largely retain their neuroepithelial morphology and adopt a final
480 cuboidal -but not squamous- appearance at a slower and species-specific pace.

481 We thus propose that RPE cell stretching versus cell addition are different solutions
482 adopted by species with different rates of development to reach a common goal: an
483 appropriate equilibrium between the surface of the RPE and that of the NR. Indeed, the
484 present study together with previous observations (27) and *in silico* models (15,65) support
485 that this equilibrium is a prerequisite for proper OV folding.

486

Key Resources Table				
Reagent type (species) or resource	Designation	Source or reference	Identifiers	Additional information
gene (<i>Danio rerio</i>)	<i>bhlhe40</i>	ENSEMBL	ENSDARG0000004060	Ref 28
Strain, strain background (<i>Oryzias latipes</i>)	Wild type, adult cab strain	CBMSO fish room		NBRP Medaka (https://shigen.nig.ac.jp/medaka/)
Strain, strain background (<i>Mus musculus</i>)	Wild type-BALB/c	CBMSO animal facility		https://www.jax.org/jax-mice-and-services
Strain, strain background (<i>Danio rerio</i>)	Adult wild type AB/tupl strain	CBMSO fish room		ZIRC (https://zebrafish.org/home/guide.ph)
Genetic reagent (<i>Danio rerio</i>)	Tg(E1-bhlhe40:GFP)	Transgenic line generated in this study.		Details in Materials and Methods, “Generation of the Tg(E1-bhlhe40:GFP) line” section
Genetic reagent (<i>Danio rerio</i>)	Tg(rx3:Gal4-VP16;UAS:GFP)	PMID:22819672	ZFIN Cat# ZDB-GENO-121105-83, RRID:ZFIN_ZDB-GENO-121105-83	Ref 48
Biological sample (<i>Homo sapiens</i>)	Paraffin sections of human embryonic eye primordia	Human Dev. Biology Resource (http://www.hdbr.org/)		
recombinant DNA reagent	ZED vector	PMID:19653328		Ref 31
recombinant DNA reagent	Bidirectional UAS:GFP	PMID: 19363289		Ref 45
recombinant DNA reagent	pQTEV-STMN1	Addgene#31326	RRID:Addgene_31326	

recombinant DNA reagent	UAS: STMN1	Construct generated in this study		Details in Materials and Methods, “Gal4-UAS-mediated expression”
recombinant DNA reagent	pCS2-Kaede	PMID: 17406330		Ref 34
recombinant DNA reagent	pCS2-H2b-mRFP	Addgene#53745	RRID:Addgene_53745	
recombinant DNA reagent	pCS2-EB3-GFP	PMID: 12684451		Ref 43
antibody	Anti-BrdU (mouse)	Becton-Dickinson		IF(1:200),
antibody	anti-GFP (chicken polyclonal)	Abcam	Cat# ab13970, RRID:AB_300798	IF(1:2000)
antibody	anti- β -catenin (Mouse monoclonal)	BD Transduction Laboratories	Cat# 610153, RRID:AB_397554	IF(1:400)
antibody	anti-ZO1 (rabbit monoclonal)	Invitrogen		IF(1:400)
antibody	Anti-laminin (rabbit polyclonal)	Sigma	Cat# L9393, RRID:AB_477163	IF(1:200)
antibody	Anti-otx2 (rabbit polyclonal)	Abcam	Cat# ab76748, RRID:AB_1524130	IF(1:1000)
antibody	Anti-Ki67 (rabbit polyclonal)	Abcam	Cat# ab15580, RRID:AB_443209	IF(1:500)
commercial assay or kit	Gateway TM LR Clonase TM Enzyme Mix	Invitrogen	11791019	
commercial assay or kit	pCR TM 8/GW/TOP O [®] TA Cloning [®] Kit	Invitrogen	K250020	
commercial assay or kit	mMessage mMachine TM SP6 transcription kit	Invitrogen	AM1340	
commercial assay or kit	NucleoSpin [®] RNA Clean-up kit	Macherey Nagel	740948.50	

Chemical compound, drug	Blebbistatin	Calbiochem	Blebbistatin-CAS674289-55-5-Calbioche,	100 μ M
chemical compound, drug	Paranitroblebbistatin	Optopharma	DR-N-111	20 μ M
chemical compound, drug	Azidoblebbistatin	Optopharma	DR-A-081	5 μ M
chemical compound, drug	Nocodazole	Sigma	M1404	10ng/ μ l
chemical compound, drug	BrdU	Roche	B23151	5mg/ml
software, algorithm	SPSS	CSIC bioinformatic resources	RRID:SCR_002865	IBM (https://www.ibm.com/uk-en/products/spss-statistics)
software, algorithm	MATLAB	CSIC bioinformatic resources	RRID:SCR_001622	MathWorks (https://www.mathworks.com/products/get-matlab.htm)
other	DAPI stain	Invitrogen	D1306	

488

489 **Animals.** Adult zebrafish (*Danio rerio*) were maintained under standard conditions at 28°C on
490 14 h-light/10 h-dark cycles. AB/Tübingen strain was used to generate the transgenic lines and
491 as control wild type. Embryos and larvae were kept in E3 medium (5 mM NaCl, 0.17 mM
492 KCl, 0.33 mM CaCl₂, 0.33 mM MgSO₄) supplemented with Methylene Blue (Sigma) at 28°C
493 and staged according to somite number and morphology (66). The lines Tg(E1-*bhlhe40*:GFP)
494 and Tg(*rx3*:Gal4;UAS:RFP) (48) lines were maintained in the same conditions and crossed to
495 generate the Tg(E1-*bhlhe40*:GFP;*rx3*:GAL4;UAS:RFP) line. Wild-type medaka fish (*Oryzias*
496 *latipes*) of the cab strain were maintained at 28°C on a 14/10-hour light/dark cycle. Embryos
497 were staged as described (67). Fertilized chick embryos (Santa Isabel Farm, Cordoba- Spain)
498 were incubated at 38°C in a humidified rotating incubator until the desired stage. Embryos
499 were inspected for normal development and staged according to (68). Wild-type BALB/c
500 mice were in pathogen-free conditions at the CBMSO animal facilities, following current
501 national and European guidelines (Directive 2010/63/EU). The day of the appearance of the

502 vaginal plug was considered as embryonic day (E)0.5. All experimental procedures were
503 approved by the CBMSO and Comunidad Autónoma de Madrid ethical committees.

504 **Human tissue.** Paraffin sections of human embryonic eye primordia were provided by the
505 Joint MRC/Wellcome Trust (grant# MR/R006237/1) Human Developmental Biology
506 Resource (<http://hdbr.org>). Sections corresponded to samples Carnegie Stage (CS) 13, 14, 15
507 and 16. CS staging allowed to determine the age of embryo as days post ovulation based on
508 morphological landmarks (69).

509 **Generation of the *Tg(E1-bhlhe40:GFP)* line.** Predictive enhancer and promoter epigenetic
510 marks (30) were used to identify different potential regulatory elements of the *bhlhe40* gene
511 (Fig. 1B). Each region was amplified by PCR with specific primers (Supplementary File 1)
512 and cloned using the pCRTM8/GW/TOPO[®] TA Cloning[®] Kit (Invitrogen). Plasmids were
513 checked for enhancer insertion and the GatewayTM LR ClonaseTM Enzyme Mix (Invitrogen)
514 was used for recombination with the ZED vector (31). The resulting constructs were injected
515 together with Tol2 mRNA to generate the corresponding transgenic embryos, which were
516 screened using a transgenesis efficiency marker present in the ZED vector (cardiac actin
517 promoter:RFP). Positive larvae were grown to adulthood (F0) and then individually
518 outcrossed with wild type partners to identify founders. Founders were analysed using
519 confocal microscopy. One of the lines corresponding to the enhancer E1 was finally selected
520 and used for subsequent studies.

521 ***Gal4-UAS-mediated expression.*** The *UAS:STMN1* construct was generated from the bi-
522 directional UAS:GFP vector, which allows simultaneous and comparable production of GFP
523 and the gene product of interest under the same regulatory sequences (45,46). The gene was
524 amplified by PCR using specific primers (Supplementary File 1) flanked by StuI restriction
525 sites and the ExpandTM High Fidelity PCR System, using the pQTEV-STMN1 (Addgene
526 #31326) construct as a mould. The PCR product was digested with StuI (Takara) and cloned
527 into the pCS2 vector and thereafter isolated together with the polyA sequence of the vector by
528 digestion with HindIII and SacII (Takara) and sub-cloned into the UAS:GFP plasmid. The
529 generated plasmid (30 pg) was injected into the *Tg(rx3:Gal4;UAS:RFP)* (48) line, together
530 with Tol2 mRNA (50 pg) to increase efficiency.

531 ***Embryos micro-injection and drug treatments.*** Embryos at one cell stage were injected using
532 a Narishige micro-injector and glass needles prepared by horizontally pulling standard

533 capillaries (filament, 1.0mm, World Precision Instruments) with aP-97 Flaming/Brown
534 Micropipette Puller (Sutter Instrument Company). A total of 30 pg for DNA and between 50
535 and 100 pg for mRNA in 1 nl volume were injected in the embryos in the cell or the yolk,
536 respectively. Drug treatments were performed on manually de-chorionated embryos at the
537 desired developmental stage in E3 medium. The following compounds were used:
538 Blebbistatin (100 μ M for 2.5 hr; Calbiochem); Paranitroblebbistatin (20 μ M; Optopharma)
539 Azidoblebbistatin (5 μ M for 15min before photoactivation; Optopharma) and Nocodazole (10
540 ng/ μ l for 2.5 hr; Sigma)

541 ***In vitro transcription.*** The pCS2:Kaede, pCS2:EB3.GFP and pCS2:H2B-RFP constructs
542 were linearized and transcribed using the mMessage mMachine™ SP6 transcription kit
543 (Invitrogen), following manufacturer's instructions. After transcription mRNAs were purified
544 using the NucleoSpin® RNA Clean-up kit (Machery Nagel).

545 ***In situ hybridization (ISH).*** *otx1* (previously known as *otx1b*) and *mitfa* probes were gifts
546 from Prof. Steve Wilson (UCL, London UK). The *bhlhe40* probe was generated by PCR from
547 24 hpf cDNA with specific primers (Supplementary File 1) using the Expand™ High Fidelity
548 PCR System. Reverse primers included the T3 promoter sequence to *in vitro* transcribe the
549 PCR product. *In vitro* transcription was performed using T3 RNA polymerase and DIG RNA
550 labelling Mix (Roche) following manufacturer's instructions. Transcription products were
551 precipitated with LiCl 0.4M and 3 volumes of ethanol 100% overnight at -20°C. Samples
552 were centrifuged at 4°C and 12000 g for 30 min, washed with ethanol 70% and re-suspended
553 in 15 μ l of RNase free water and 15 μ l Ultra-Pure Formamide (Panreac). ISH were
554 performed as described (70).

555 ***BrdU incorporation assays.*** BrdU (5-Bromo-2'-deoxyuridine, Roche) was re-suspended in
556 DMSO (Sigma) to generate stocks of 50 mg/ml that were kept at -20°C. For Tg(E1-
557 *bhlhe40*:GFP) zebra- and wild type medaka fish groups of 15 embryos of stages comprised
558 between 16 ss and 48 hpf were dechorionated and placed in BrdU solution (5 mg/ml in E3
559 medium) for 30 min on ice and then washed with fresh E3 medium. Embryos were let recover
560 at 28°C for 10 min before fixation in PFA 4% overnight at 4°C. For analysis in chick, BrdU
561 (50 mg/egg) was added to each embryo 30 min before fixation. For analysis in mouse,
562 pregnant dams were injected intraperitoneally with BrdU (50 μ g/g), sacrificed 1hr later and
563 fixed. Chick and mouse embryos were immersion fixed in 4% paraformaldehyde in 0.1 M
564 phosphate buffer, pH 7 at 4°C for 4hr and then washed in PBS and cryoprotected in 15% and

565 30% saccharose in 0.1 M phosphate buffer. All embryos were cryo-sectioned and the sections
566 hydrated with PBS 1X during 5 min and incubated in HCl during 40 minutes at 37°C. After
567 HCl treatment, sections were rinsed with PBS 1X ten times, and then processed for
568 immunofluorescence as described below. The percentage of RPE proliferating progenitors
569 was determined as the proportion of BrdU positive cells over the total number of GFP (for
570 E1-*bhlhe40*:GFP) or Otx2/Hoechst (medaka fish, chick, mouse embryos) positive cells in the
571 RPE layer in each section. A minimum of three embryos and sections per embryo were
572 counted (both eyes).

573 **Immunofluorescence.** Zebrafish embryos at the corresponding stage for each experiment
574 were fixed with 4% (w/vol) paraformaldehyde (PFA, Merck) in 0.1 M phosphate buffer
575 overnight at 4°C. Whole-mount immunofluorescence was performed as described (70).
576 Alternatively, embryos were incubated in 15% sucrose - PBS overnight at 4°C, embedded in
577 7.5% gelatine (Sigma) 15% sucrose (Merck), frozen in isopentane (PanReac) between -30 and
578 -40°C and kept at -80°C. Cryo-sectioning was performed with a cryostat (Leica CM 1950) at
579 20 µm thickness and dried overnight at RT. Chick and mouse embryos were collected, fixed
580 4% paraformaldehyde, equilibrated in sucrose and cryo-sectioned as above. Paraffin sections
581 of human embryonic tissue were de-paraffinized, washed in PBS, processed for antigen
582 retrieval (10mM citrate buffer, pH6, for 5min at 110°C in a boiling chamber, Biocaremedical)
583 and subsequently processed together with all other samples for immunofluorescence.
584 Immunostaining was performed as described (70) using the following primary antibodies:
585 mouse anti-BrdU (1:200; Becton-Dickinson); chick anti-GFP (1:2000; Abcam); mouse anti-
586 βcatenin (1:400, BD transduction Laboratories); mouse anti-ZO-1 (1:400, Invitrogen); rabbit
587 anti-laminin (1:200, Sigma); rabbit anti-Otx2 antibodies (1:1000; Abcam) rabbit anti-Ki67
588 (1:500, Abcam). The used secondary antibodies were conjugated with Alexa 488, Alexa-594
589 or Alexa-647 (1:500; Thermo Fisher). Sections were counterstained with Hoechst
590 (Invitrogen), mounted in Mowiol and analysed by conventional and confocal microscopy.

591 **Kaede photoconversion.** Wild type embryos were injected with Kaede mRNA. Embryos at 15
592 hpf with homogeneous green fluorescence were selected, mounted and visualized under the
593 Nikon AR1+ Confocal Microscope using a 20X/0.75 Plan-Apochromat objective. A region of
594 interest (ROI) was drawn in the outer layer, corresponding to the putative position of the RPE
595 progenitors, at a specific z position and irradiated with the 405 nm laser at 21% of power for
596 10 loops to switch Kaede emission from green to red fluorescence. Due to confocality, photo-
597 conversion occasionally extended further than the selected plane, so that the tissues present

598 above or below (i.e. ectoderm) also underwent photo-conversion. After photo-conversion
599 embryos were let develop up to approx. 30 hpf stage, fixed and analysed by confocal
600 microscopy for red fluorescence distribution.

601 ***Azidoblebbistatin photoactivation.*** Azido-blebbistatin (Ableb) (39) was photoactivated with a
602 Zeiss LSM 780 Upright multiphoton FLIM system with a W Plan-Apochromat 20x/1,0 DIC
603 M27 75 mm WD 1.8 mm dipping objective. For each eye a specific ROI was drawn including
604 RPE cells identified by GFP fluorescence. Ableb was activated in the ROIs using 860 nm
605 wave-length and 20 mW laser power (this corresponds to 9-14 $\mu\text{W}/\mu\text{m}^2$ inside the ROI).

606 ***Confocal imaging.*** Embryos were mounted with the appropriate orientation in 1.5% low
607 melting point agarose (Conda) diluted in E3 medium (for in vivo recording) or PBS (for fixed
608 samples). Images were acquired either with a Nikon A1R+ High Definition Resonant
609 Scanning Confocal Microscope connected to an Inverted Eclipse Ti-E Microscope (20X/0.75
610 Plan-Apochromat, 40X/1.3 oil Plan-Fluor and 60X/1.4 oil Plan-Apocromat objectives) or
611 with a Zeiss LSM710 Confocal Laser Scanning Microscope connected to a Vertical
612 AxioImager M2 Microscope (40X/1.3 oil Plan-Apochromat, W N-Achroplan 20x/0.5, W
613 Plan-Apochromat 40x/1.0 DIC VIS-IR).

614 ***3D reconstructions.*** 3D Videos (i.e. Video 1-3) were generated from full stacks using the 3D
615 project option in Fiji (71). RPE surface renderings were generated using Imaris (Bitplane),
616 with a value of 6 in Surface Area Detail and 7 in Background Subtraction.

617 ***Morphometric analysis.*** Unless otherwise specified, morphometric analysis of cells and
618 tissues was performed using Matlab© (The Mathworks©, Natick, MA) using the XYZ
619 coordinates of the processed images or Fiji (71). This analysis was performed using
620 previously processed fluorescent images from videos of Tg(E1-*bhlhe40*:GFP;
621 *rx3*:GAL4;UAS:RFP) or Tg(E1-*bhlhe40*:GFP) and H2B-RFP-injected embryos (Video 2 and
622 4), from which the signal corresponding to the RPE or the whole OV/OC were isolated semi-
623 manually with the help of Fiji macros and tools designed to select 3D structures. The RPE
624 specific GFP signal was processed with a median filter. In the case of Video 4, the
625 background ramp for the GFP signal was neutralized in each frame via subtraction of a copy
626 of itself after a grey-scale morphological operation (72,73). For all videos, the median
627 intensity was thereafter established as the cut off value for differentiating background and
628 signal (i.e. pixel with an intensity lower than the cut off were set to zero) for all images that
629 were in both videos. The signal derived from H2B was localized in cell nuclei, and therefore

630 it was post-processed with a grey-scale closing operation to fill empty spaces between nuclei.
631 Morphometric analysis was performed in the resulting processed images. All values were
632 calculated in microns by scaling the x, y, z coordinates according to the follow: (0.62 μm x
633 0.62 μm x 1.37 μm) for Video 2 and (0.62 μm x 0.62 μm x 1.07 μm) for Video 4. Volumes (μm^3)
634 were calculated as the number of voxels with a value higher than zero. RPE surface (μm^2) was
635 calculated applying a second order linear adjustment on the plane YZ corresponding to the
636 plane of the OV/OC hinges with the fit function available in Matlab© (The Mathworks©,
637 Natick, MA). RPE thickness (μm) was determined as the result of volume (μm^3)/surface
638 (μm^2). Unfortunately, semi-manual RPE image extraction was not perfect, when GFP-signal
639 associated to CMZ development arise. To account for this problem, the GFP signal for each
640 frame was divided into seven equivalent blocks using the x,y coordinates from the z-
641 projection of each frame. In this case, RPE volume and surface were calculated independently
642 in each one of the regions up to 20 hpf, when the most anterior block (now corresponding to
643 the arising CMZ) was discarded from the analysis. For the subsequent frames the two anterior
644 most blocks were discarded (Figure 3-figure supplement 1). The total OV/OC volume (μm^3)
645 was determined using the red fluorescence from the Tg(rx3:GAL4;UAS:RFP) embryos at 17-
646 22hpf. H2B expression was used to determine the volume of the optic cup (H2B volume in
647 Fig. 3) as follows for each frame of the Video 4: the maximum, gaussian blur and minimum
648 filters were applied to the image; subsequently, the convex hull (68) was calculated for the
649 image to obtain the geometrical shape that covers all pixels with an intensity higher than zero,
650 including the lens; finally, only the regions present in the image and the convex hull are used
651 to define the H2B volume. Individual cell area was determined in cells located at a medial
652 position of the OV for each cell type (progenitor, RPE and NR); cell contour was drawn using
653 the segmented line tool in Fiji (71). Apico-basal (A-B) length (μm) of individual cells was
654 estimated by manually tracing a line from the basal to the apical membrane in the z position
655 in which the nucleus had its larger surface using the straight-line tool in Fiji (71). To account
656 for possible developmental asynchrony when eyes from the same embryo were differentially
657 treated (irradiated vs. non-irradiated), the A-B length of the irradiated eye was normalized
658 with that of the non-irradiated eye. Values above 1 indicated less RPE cell flattening in
659 experimental eyes. The invagination angle was determined as previously described (13) using
660 manual drawing with the Fiji angle tool (71). The vertex of the angle was placed
661 approximately in the centre of the basal surface of the NR and the vectors were drawn up to
662 the edges of the CMZ. Angles were measured in the z positions in which the irradiated RPE
663 was maximally affected and compared to equivalent positions of control non-irradiated eyes.

664 Values were normalized with those of the contralateral non-treated eye, to account for
665 possible asynchronies.

666 ***Statistical analysis.*** All statistical analysis was performed with IBM SPSS Statistics Version
667 20.0. The method used is indicated in each case together with the sample size.

668

669 **Data Availability.** All data generated or analysed during this study are included in the
670 manuscript and supporting files. Source data files have been provided for all the graphs
671 shown in the study.

672 **Acknowledgements.** We wish to thanks Drs JR Martinez-Morales and E. Marti for critical
673 reading the manuscript; the confocal microscopy service of the CBMSO and CNIC (Centro
674 Nacional de Investigaciones Cardiovasculares) for help with image acquisition and analysis
675 and the fish facilities for caring of the zebrafish lines. This work was supported by grants
676 from the Spanish AEI (BFU2014-55918-P to FC; BFU2016-75412-R with FEDER support,
677 RED2018-102553-T and PID2019-104186RB-100 to PB), BBVA Foundation
678 (N[16]_BBM_BAS_0078 to FC) and Fundación Ramon Areces-2016 (to PB). TMM and ML
679 were supported by FPU (FPU14/02867) and FPI (BES-2015-073253) pre-doctoral contracts
680 from the Spanish AEI, respectively. We also acknowledge a CBM Institutional grant from the
681 Fundación Ramon Areces.

682 **Competing interest:** The authors declare no competing interests

683

684 **References**

685

- 686 1. Letelier J, Bovolenta P, Martínez-Morales JR. The pigmented epithelium, a bright partner against
687 photoreceptor degeneration. *Journal of Neurogenetics*. 2017 Oct 2;31(4):203–15.
- 688 2. Moreno-Marmol T, Cavodeassi F, Bovolenta P. Setting Eyes on the Retinal Pigment Epithelium.
689 *Front Cell Dev Biol*. 2018;6:145.
- 690 3. Li Z, Joseph NM, Easter SS. The morphogenesis of the zebrafish eye, including a fate map of the optic
691 vesicle. *Dev Dyn*. 2000 May;218(1):175–88.
- 692 4. Gallardo V, Bovolenta P. Positive and negative regulation of Shh signalling in vertebrate retinal
693 development. *F1000Res*. 2018;7.
- 694 5. Cardozo MJ, Almuedo-Castillo M, Bovolenta P. Patterning the Vertebrate Retina with Morphogenetic
695 Signaling Pathways. *Neuroscientist*. 2020 Apr;26(2):185–96.
- 696 6. Beccari L, Marco-Ferreres R, Bovolenta P. The logic of gene regulatory networks in early vertebrate
697 forebrain patterning. *Mech Dev*. 2013 Feb;130(2–3):95–111.
- 698 7. Buono L, Martinez-Morales JR. Retina Development in Vertebrates: Systems Biology Approaches to
699 Understanding Genetic Programs: On the Contribution of Next-Generation Sequencing Methods to the
700 Characterization of the Regulatory Networks Controlling Vertebrate Eye Development. *Bioessays*.
701 2020 Apr;42(4):e1900187.
- 702 8. Buono L., Corbacho J, Naranjo S, Almuedo-Castillo M, Moreno-Marmol T, de la Cerda B, Sanbria-
703 Reinoso E, Polvillo R, Díaz-Corrales FJ, Bogdanovic O, Bovolenta P, Martínez-Morales JR, Analysis
704 of gene network bifurcation during optic cup morphogenesis in zebrafish. *Nat Commun*. 2021 Jun
705 23;12(1):3866.
- 706 9. Martinez-Morales JR, Cavodeassi F, Bovolenta P. Coordinated Morphogenetic Mechanisms Shape the
707 Vertebrate Eye. *Front Neurosci*. 2017 11:721.
- 708 10. Martinez-Morales JR, Rembold M, Greger K, Simpson JC, Brown KE, Quiring R, et al. ojolano-
709 mediated basal constriction is essential for optic cup morphogenesis. *Development*. 2009
710 Jul;136(13):2165–75.
- 711 11. Nicolas-Perez M, Kuchling F, Letelier J, Polvillo R, Wittbrodt J, Martinez-Morales JR. Analysis of
712 cellular behavior and cytoskeletal dynamics reveal a constriction mechanism driving optic cup
713 morphogenesis. *Elife*. 2016 Oct 31;5.
- 714 12. Bryan CD, Chien CB, Kwan KM. Loss of laminin alpha 1 results in multiple structural defects and
715 divergent effects on adhesion during vertebrate optic cup morphogenesis. *Dev Biol*. 2016 Aug
716 15;416(2):324–37.
- 717 13. Sidhaye J, Norden C. Concerted action of neuroepithelial basal shrinkage and active epithelial
718 migration ensures efficient optic cup morphogenesis. *Elife*. 2017 Apr 4;6.
- 719 14. Eiraku M, Takata N, Ishibashi H, Kawada M, Sakakura E, Okuda S, et al. Self-organizing optic-cup
720 morphogenesis in three-dimensional culture. *Nature*. 2011 06/online;472:51.
- 721 15. Okuda S, Takata N, Hasegawa Y, Kawada M, Inoue Y, Adachi T, et al. Strain-triggered mechanical
722 feedback in self-organizing optic-cup morphogenesis. *Sci Adv*. 2018 Nov;4(11):eaau1354.
- 723 16. Li Zheng, Hu Minjie, Ochocinska Malgorzata J, Joseph Nancy M, Easter Stephen S. Modulation of
724 cell proliferation in the embryonic retina of zebrafish (*Danio rerio*). *Dev Dyn*. 2000 219(3):391–401.
- 725 17. Heermann S, Schutz L, Lemke S, Krieglstein K, Wittbrodt J. Eye morphogenesis driven by epithelial
726 flow into the optic cup facilitated by modulation of bone morphogenetic protein. *Elife*. 2015 Feb 24;4.
- 727 18. Kwan KM, Otsuna H, Kidokoro H, Carney KR, Saijoh Y, Chien CB. A complex choreography of cell
728 movements shapes the vertebrate eye. *Development*. 2012 Jan;139(2):359–72.
- 729 19. Picker A, Cavodeassi F, Machate A, Bernauer S, Hans S, Abe G, et al. Dynamic Coupling of Pattern
730 Formation and Morphogenesis in the Developing Vertebrate Retina. *PLOS Biology*.

- 731 2009;7(10):e1000214.
- 732 20. Bryan CD, Casey MA, Pfeiffer RL, Jones BW, Kwan KM. Optic cup morphogenesis requires neural
733 crest-mediated basement membrane assembly. *Development*. 2020 Feb 21;147(4).
- 734 21. Martinez-Morales JR, Rodrigo I, Bovolenta P. Eye development: a view from the retina pigmented
735 epithelium. *Bioessays*. 2004 Jul;26(7):766–77.
- 736 22. Cechmanek PB, McFarlane S. Retinal pigment epithelium expansion around the neural retina occurs
737 in two separate phases with distinct mechanisms. *Dev Dyn*. 2017 Aug;246(8):598–609.
- 738 23. Martinez-Morales JR, Signore M, Acampora D, Simeone A, Bovolenta P. Otx genes are required for
739 tissue specification in the developing eye. *Development*. 2001;128(11):2019–30.
- 740 24. Bharti K, Nguyen MT, Skuntz S, Bertuzzi S, Arnheiter H. The other pigment cell: specification and
741 development of the pigmented epithelium of the vertebrate eye. *Pigment Cell Res*. 2006
742 Oct;19(5):380–94.
- 743 25. Kim JY, Park R, Lee JHJ, Shin J, Nickas J, Kim S, et al. Yap is essential for retinal progenitor cell
744 cycle progression and RPE cell fate acquisition in the developing mouse eye. *Developmental Biology*.
745 2016 Nov 15;419(2):336–47.
- 746 26. Nakano T, Ando S, Takata N, Kawada M, Muguruma K, Sekiguchi K, et al. Self-Formation of Optic
747 Cups and Storable Stratified Neural Retina from Human ESCs. *Cell Stem Cell*. 2012 Jun
748 14;10(6):771–85.
- 749 27. Carpenter AC, Smith AN, Wagner H, Cohen-Tayar Y, Rao S, Wallace V, et al. Wnt ligands from the
750 embryonic surface ectoderm regulate ‘bimetallic strip’ optic cup morphogenesis in mouse.
751 *Development*. 2015;142(5):972–82.
- 752 28. Yamada K, Miyamoto K. Basic helix-loop-helix transcription factors, BHLHB2 and BHLHB3; their
753 gene expressions are regulated by multiple extracellular stimuli. *Front Biosci*. 2005 Sep 1;10:3151–71.
- 754 29. Yao J, Wang L, Chen L, Zhang S, Zhao Q, Jia W, et al. Cloning and developmental expression of the
755 DEC1 ortholog gene in zebrafish. *Gene Expr Patterns*. 2006 Oct;6(8):919–27.
- 756 30. Bogdanovic O, Fernandez-Minan A, Tena JJ, de la Calle-Mustienes E, Hidalgo C, van Kruysbergen I,
757 et al. Dynamics of enhancer chromatin signatures mark the transition from pluripotency to cell
758 specification during embryogenesis. *Genome Res*. 2012 Oct;22(10):2043–53.
- 759 31. Bessa J, Tena JJ, de la Calle-Mustienes E, Fernandez-Minan A, Naranjo S, Fernandez A, et al.
760 Zebrafish enhancer detection (ZED) vector: a new tool to facilitate transgenesis and the functional
761 analysis of cis-regulatory regions in zebrafish. *Dev Dyn*. 2009 Sep;238(9):2409–17.
- 762 32. Zou J, Beermann F, Wang J, Kawakami K, Wei X. The Fugu *tyrp1* promoter directs specific GFP
763 expression in zebrafish: tools to study the RPE and the neural crest-derived melanophores. *Pigment
764 Cell Res*. 2006 Dec;19(6):615–27.
- 765 33. Miesfeld JB, Link BA. Establishment of transgenic lines to monitor and manipulate Yap/Taz-Tead
766 activity in zebrafish reveals both evolutionarily conserved and divergent functions of the Hippo
767 pathway. *Mech Dev*. 2014 Aug;133:177–88.
- 768 34. Ando R, Hama H, Yamamoto-Hino M, Mizuno H, Miyawaki A. An optical marker based on the UV-
769 induced green-to-red photoconversion of a fluorescent protein. *Proc Natl Acad Sci U S A*. 2002 Oct
770 1;99(20):12651–6.
- 771 35. Totaro A, Panciera T, Piccolo S. YAP/TAZ upstream signals and downstream responses. *Nat Cell
772 Biol*. 2018 Aug;20(8):888–99.
- 773 36. Tee SY, Fu J, Chen CS, Janmey PA. Cell shape and substrate rigidity both regulate cell stiffness.
774 *Biophys J*. 2011 Mar 2;100(5):L25–7.
- 775 37. Vishavkarma R, Raghavan S, Kuyyamudi C, Majumder A, Dhawan J, Pullarkat PA. Role of actin
776 filaments in correlating nuclear shape and cell spreading. *PLoS One*. 2014;9(9):e107895.
- 777 38. Rauscher AA, Gyimesi M, Kovacs M, Malnasi-Csizmadia A. Targeting Myosin by Blebbistatin
778 Derivatives: Optimization and Pharmacological Potential. *Trends Biochem Sci*. 2018 Sep;43(9):700–

- 779 13.
- 780 39. Kepiro M, Varkuti BH, Bodor A, Hegyi G, Drahos L, Kovacs M, et al. Azidoblebbistatin, a
781 photoreactive myosin inhibitor. *Proc Natl Acad Sci U S A*. 2012 Jun 12;109(24):9402–7.
- 782 40. Kepiro M, Varkuti BH, Rauscher AA, Kellermayer MSZ, Varga M, Malnasi-Csizmadia A. Molecular
783 tattoo: subcellular confinement of drug effects. *Chem Biol*. 2015 Apr 23;22(4):548–58.
- 784 41. Yevick HG, Martin AC. Quantitative analysis of cell shape and the cytoskeleton in developmental
785 biology. *Wiley Interdiscip Rev Dev Biol*. 2018 Nov;7(6):e333.
- 786 42. Pope KL, Harris TJ. Control of cell flattening and junctional remodeling during squamous epithelial
787 morphogenesis in *Drosophila*. *Development*. 2008 Jul;135(13):2227–38.
- 788 43. Stepanova T, Slemmer J, Hoogenraad CC, Lansbergen G, Dortland B, De Zeeuw CI, et al.
789 Visualization of microtubule growth in cultured neurons via the use of EB3-GFP (end-binding protein
790 3-green fluorescent protein). *J Neurosci*. 2003 Apr 1;23(7):2655–64.
- 791 44. Belmont LD, Mitchison TJ. Identification of a protein that interacts with tubulin dimers and increases
792 the catastrophe rate of microtubules. *Cell*. 1996 Feb 23;84(4):623–31.
- 793 45. Paquet D, Bhat R, Sydow A, Mandelkow E-M, Berg S, Hellberg S, et al. A zebrafish model of
794 tauopathy allows in vivo imaging of neuronal cell death and drug evaluation. *J Clin Invest*. 2009
795 May;119(5):1382–95.
- 796 46. Distel M, Hocking JC, Volkmann K, Koster RW. The centrosome neither persistently leads migration
797 nor determines the site of axonogenesis in migrating neurons in vivo. *J Cell Biol*. 2010 Nov
798 15;191(4):875–90.
- 799 47. Bovolenta P, Mallamaci A, Briata P, Corte G, Boncinelli E. Implication of OTX2 in pigment
800 epithelium determination and neural retina differentiation. *J Neurosci*. 1997 Jun 1;17(11):4243–52.
- 801 48. Weiss O, Kaufman R, Michaeli N, Inbal A. Abnormal vasculature interferes with optic fissure closure
802 in *lmo2* mutant zebrafish embryos. *Dev Biol*. 2012 Sep 15;369(2):191–8.
- 803 49. Furutani-Seiki M, Wittbrodt J. Medaka and zebrafish, an evolutionary twin study. *Mech Dev*. 2004
804 Jul;121(7–8):629–37.
- 805 50. O’Rahilly R. The timing and sequence of events in the development of the human eye and ear during
806 the embryonic period proper. *Anat Embryol*. 1983;168(1):87–99.
- 807 51. Goldsmith TH. Optimization, constraint, and history in the evolution of eyes. *Q Rev Biol*. 1990
808 Sep;65(3):281–322.
- 809 52. Cohen-Tayar Y, Cohen H, Mitiagin Y, Abravanel Z, Levy C, Idelson M, et al. Pax6 regulation of
810 Sox9 in the mouse retinal pigmented epithelium controls its timely differentiation and choroid
811 vasculature development. *Development*. 2018 09;145(15).
- 812 53. Hu Y, Wang X, Hu B, Mao Y, Chen Y, Yan L, et al. Dissecting the transcriptome landscape of the
813 human fetal neural retina and retinal pigment epithelium by single-cell RNA-seq analysis. *PLOS*
814 *Biology*. 2019 Jul 3;17(7):e3000365.
- 815 54. Abe T, Ishikawa T, Masuda T, Mizusawa K, Tsukamoto T, Mitani H, et al. Molecular analysis of
816 Dec1 and Dec2 in the peripheral circadian clock of zebrafish photosensitive cells. *Biochem Biophys*
817 *Res Commun*. 2006 Dec 29;351(4):1072–7.
- 818 55. Fuhrmann S, Zou C, Levine EM. Retinal pigment epithelium development, plasticity, and tissue
819 homeostasis. *Experimental Eye Research*. 2014 Jun 1;123:141–50.
- 820 56. Leask A, Byrne C, Fuchs E. Transcription factor AP2 and its role in epidermal-specific gene
821 expression. *Proc Natl Acad Sci USA*. 1991 Sep 15;88(18):7948–52.
- 822 57. Pearson RA, Catsicas M, Becker DL, Bayley P, Lüneborg NL, Mobbs P. Ca(2+) signalling and gap
823 junction coupling within and between pigment epithelium and neural retina in the developing chick.
824 *Eur J Neurosci*. 2004 May;19(9):2435–45.
- 825 58. Bao H, Yang S, Li H, Yao H, Zhang Y, Zhang J, et al. The Interplay Between E-Cadherin, Connexin
826 43, and Zona Occludens 1 in Retinal Pigment Epithelial Cells. *Invest Ophthalmol Vis Sci*. 2019 Dec

827 2;60(15):5104–11.

828 59. Buskila Y, Bellot-Saez A, Morley JW. Generating Brain Waves, the Power of Astrocytes. *Front*
829 *Neurosci.* 2019;13:1125.

830 60. Gurdon JB. A community effect in animal development. *Nature.* 1988 Dec 22;336(6201):772–4.

831 61. Nguyen M, Arnheiter H. Signaling and transcriptional regulation in early mammalian eye
832 development: a link between FGF and MITF. *Development.* 2000;127(16):3581–91.

833 62. Lane BM, Lister JA. Otx but not Mitf transcription factors are required for zebrafish retinal pigment
834 epithelium development. *PLoS One.* 2012;7(11):e49357.

835 63. Miesfeld JB, Gestri G, Clark BS, Flinn MA, Poole RJ, Bader JR, et al. Yap and Taz regulate retinal
836 pigment epithelial cell fate. *Development.* 2015 Sep 1;142(17):3021–32.

837 64. Martinez-Morales J-R, Del Bene F, Nica G, Hammerschmidt M, Bovolenta P, Wittbrodt J.
838 Differentiation of the vertebrate retina is coordinated by an FGF signaling center. *Dev Cell.* 2005
839 Apr;8(4):565–74.

840 65. Eiraku M, Adachi T, Sasai Y. Relaxation-expansion model for self-driven retinal morphogenesis: a
841 hypothesis from the perspective of biosystems dynamics at the multi-cellular level. *Bioessays.* 2012
842 Jan;34(1):17–25.

843 66. Kimmel CB, Ballard WW, Kimmel SR, Ullmann B, Schilling TF. Stages of embryonic development
844 of the zebrafish. *Dev Dyn.* 1995 Jul;203(3):253–310.

845 67. Iwamatsu T. Stages of normal development in the medaka *Oryzias latipes*. *Mech Dev.* 2004
846 Jul;121(7–8):605–18.

847 68. Hamburger V, Hamilton HL. A series of normal stages in the development of the chick embryo. 1951.
848 *Dev Dyn.* 1992 Dec;195(4):231–72.

849 69. O’Rahilly R, Müller F. Developmental stages in human embryos: revised and new measurements.
850 *Cells Tissues Organs (Print).* 2010;192(2):73–84.

851 70. Cardozo MJ, Sanchez-Arrones L, Sandonis A, Sanchez-Camacho C, Gestri G, Wilson SW, et al. Cdon
852 acts as a Hedgehog decoy receptor during proximal-distal patterning of the optic vesicle. *Nat*
853 *Commun.* 2014 Jul 8;5:4272.

854 71. Schindelin J, Arganda-Carreras I, Frise E, Kaynig V, Longair M, Pietzsch T, et al. Fiji: an open-source
855 platform for biological-image analysis. *Nat Methods.* 2012 Jun 28;9(7):676–82.

856 72. Hassanpour H, Samadiani N, Mahdi Salehi SM. Using morphological transforms to enhance the
857 contrast of medical images. *The Egyptian Journal of Radiology and Nuclear Medicine.* 2015 Jun
858 1;46(2):481–9.

859 73. Arce GR. *Nonlinear Signal Processing: A Statistical Approach.* John Wiley & Sons; 2005. 484 p.

860

861

862 **Figure legends**

863

864 **Figure 1. The Tg(E1-*bhlhe40*:GFP) line is a suitable tool to study early RPE generation.**

865 **A)** Frontal cryo-sections of 14-24 hpf wt embryos hybridized *in toto* with a *bhlhe40* specific
866 probe. mRNA is first detected in the dorsal most region of the OV outer layer (arrowhead)
867 and then expands ventrally. **B)** UCSC Genome Browser view of H3K27ac (purple, potential
868 active enhancers), H3K4me3 (green, potentially active promoters) and H3K36me3 (light blue,
869 transcriptionally active regions) tracks obtained for four zebrafish developmental stages:
870 dome, 80% epiboly, 24 hpf, 48 hpf related to the upstream *bhlhe40* genomic locus (50kb).
871 The black arrow at the bottom indicates *bhlhe40* position and direction. The promoter (P) and
872 the four selected enhancers (E1 to E4) are highlighted with a color-coded box. **C)** Time-
873 frames from *in vivo* time-lapse recording of a Tg(E1-*bhlhe40*:GFP;*rx3*:GAL4;UAS;RFP)
874 embryo between 14-24 hpf. Time is indicated in min. Note that the GFP reporter signal
875 matches the *bhlhe40* mRNA distribution in A. **D)** 3D reconstruction of the prospective RPE
876 from Tg(E1-*bhlhe40*:GFP) embryos at the stages indicated in the panel. **E)** Dorsal view of a
877 wt embryo injected with Kaede mRNA (green) at 12 hpf. A group of cells in the dorsal region
878 of the outer layer was photoconverted (magenta, panel on the left) and the embryo visualized
879 at 30 hpf (right panel). Magenta labelled cells cover the entire RPE region. Black and white
880 dashed lines delineate the OV, neural tube and virtual lumen in **A**, **C**. Abbreviations: A,
881 anterior; cmz, ciliary margin zone; il, inner layer; l, lateral; m, medial; NR, NR; OC, OC; ol,
882 outer layer; OV, optic vesicle; P, posterior; RPE, retinal pigment epithelium. Scale bars: 100
883 μm (A-D); 50 μm , E.

884

885 **Figure 2. The RPE converts from a pseudostratified to a squamous epithelium during**

886 **OV folding by increasing individual cell surface. A-C')** Confocal images of frontal cryo-
887 sections of Tg(E1-*bhlhe40*:GFP) embryos immunostained for GFP (green) and β -catenin
888 (white) and counterstained with Hoechst (blue). Note that the RPE rapidly decreases its
889 thickness (white straight line in **A-C**) and cells change from columnar (14 hpf, arrow in **A'**) to
890 cuboidal (16 hpf, arrow in **B'**) and then flat shape (22 hpf, arrow in **C'**). White dashed lines
891 delineate eye contour and virtual lumen in A-C. **D-E')** Confocal images of the posterior RPE
892 (D, D') and NR (E, E') regions of an eye cup dissected from 30 hpf Tg(E1-*bhlhe40*:GFP)
893 embryos immunostained for GFP (green) and β -catenin (white) and counterstained with
894 Hoechst (blue). Images in D', E' are high power views of the areas boxed in white box in D,
895 E. Note the hexagonal morphology (yellow arrow in D') of RPE cells (average area $354.8 \pm$

896 100.3 μm^2) in contrast to the small and roundish cross-section of retinal progenitors (average
897 area $22.5 \pm 2.9 \mu\text{m}^2$; yellow arrow in E'). **F)** The graph represents the average area of
898 individual OV progenitors and NR and RPE cells (n= 15-19). The average area is calculated
899 using cells from 5 different embryos. Data represent mean \pm SD, **** p<0.0001. ns non-
900 significant. Scale bar: 50 μm .

901

902 **Figure 3-figure supplement 1. RPE region selection from the GFP positive domain. A)**
903 3D reconstruction of the frames at 18, 19.7 and 21.5 hpf from the Video 1. The analysed GFP
904 positive domain are depicted in green whereas those in turquoise have been excluded when
905 calculating the RPE volume plotted in Fig. 3A. The *rx3* positive domain is depicted in pink.
906 **B)** RPE volume bar plot. Light and dark green colours illustrate the total GFP positive volume
907 of the central RPE and CMZ region respectively. The dark green region has been excluded to
908 calculate the total volume.

909 **Figure 3. RPE volume is conserved during initial tissue morphogenesis. A)** Image on the
910 left represents the reconstruction of a single frame from Video 2 (Tg(E1-*bhlhe40*:GFP;
911 *rx3*:GAL4;UAS:RFP embryo) showing the OV/OC in red and the RPE in green. The
912 segments in which the RPE was discretized are depicted with black dashed lines. The image
913 on the right shows the RPE reconstruction obtained after filtering. Double arrow points to
914 RPE thickness. **B-D)** The graphs show how the RPE thickness (B, calculated as
915 volume/surface), surface (C) and volume (D) change as a function of the developmental stage.
916 **E)** 3D reconstructions of raw (left) and processed (right) versions of a frame from the Video
917 1-2. **F)** 3D reconstructions of raw (left) and processed (right) versions of a frame from the
918 Video 4. **G)** Quantification of RPE and eye volume based on Video 1-2 (*rx3* volume
919 quantification) and the Video 4 (H2B volume quantification) along developmental stages.

920

921 **Figure 4. RPE flattening is a myosin-dependent cell-autonomous process required for**
922 **proper OV folding. A-J)** Confocal images of dorsally viewed Tg(E1-*bhlhe40*:GFP) embryos
923 before (17 hpf; **A)** and 2.5 hr after incubation (19.5 hpf) with either DMSO (**B, E, H**),
924 Blebbistatin (**C**), p-nitro-Blebbistatin (**D**) or ABleb (**F, G, I, J**) with (**G, J**) or without
925 irradiation (**F, I**) in the prospective RPE (**F-G**) or NR (**I-J**). Images in E', F', G' H', I' and J'
926 are high power views of RPE morphology. Embryos were immunostained for GFP (green), β -
927 catenin (white) and counterstained with Hoechst (blue). Note that the OC forms and the RPE
928 flattens (white arrowhead in B) normally in all DMSO treated embryos (**B, E, E', H, H'**) or in

929 embryos incubated in Ableb without irradiation (F, F', I, I'). In contrast, the RPE remains
930 cuboidal (white arrowhead in C) and NR cells seem not undergo basal constriction (yellow
931 arrowhead in C) in the presence of myosin inhibitors (C, D). Photo-activation of Ableb in the
932 RPE prevents cell flattening (compare E',F' with G') and impairs OV folding (G). When
933 Ableb is photo-activated in the NR, folding of the OV is also impaired (J) but RPE cells
934 undergo flattening (compare H',I' with J'). The number of embryos analysed and showing the
935 illustrated phenotype is indicated on the top right corner of each panel and the average
936 invagination angle and mean A-B on the left bottom corner. The yellow dashed line in **E, H**
937 indicate how the invagination angle (α) was determined. (**K, M**) Normalized RPE height in
938 DMSO and Ableb treated embryos, irradiated either in the RPE (K) or in the NR (M). (**L, N**)
939 Normalized invagination angle in DMSO and Ableb treated embryos irradiated either in the
940 RPE (L) or in the NR (N). Data represent mean \pm SD; ** $p < 0.01$ and *** $p < 0.001$. ns non-
941 significant. Scale bars: 50 μ m in A-J and 25 μ m in E'-J.'

942

943 **Figure 5-figure supplement 1. EB3-GFP dynamics during RPE cell remodelling. A-C)**
944 Frames from representative Video 5 showing the orientation of microtubule dynamics in RPE
945 cells with a neuroepithelial (A, continuous acquisition, n = 9), cuboidal (B, continuous
946 acquisition, n = 10) and squamous conformation (C, continuous acquisition, n = 15). Insets
947 provide higher power view of the three images. Scale bar 25 μ m

948

949 **Figure 5. Microtubule dynamics is required for RPE cell flattening and OV folding. A-**
950 **F)** Confocal images of dorsally viewed Tg(E1-*bhlhe40*:GFP) embryos before (16 hpf, A; 17
951 hpf D) and 2.5 hr after incubation (18.5 hpf B, C; 19.5 hpf E,F) with either DMSO (B, E) or
952 Nocodazole (C, F). Embryos were immunostained for GFP (green, A-F), β -catenin (white, D-
953 F) and counterstained with Hoechst (blue). Note that the OC forms and the RPE flattens
954 (white arrowhead in B, E) normally in DMSO treated embryos. RPE cells retain a columnar-
955 like morphology in the presence of Nocodazole (white arrowhead in C, F). In embryos treated
956 at earlier stage, the NR seems to bend outward (yellow arrowhead in C), whereas some
957 folding occurs when the embryos are treated at later stages (yellow arrowhead in F), although
958 cells seems to accumulate at the hinge (thin white arrowhead, F). The number of embryos
959 analysed and showing the illustrated phenotype is indicated on the top right corner of each
960 panel. **G, H)** Confocal images of dorsally viewed *rx3*:GAL4;UAS;RFP embryos injected with
961 the UAS:GFP (G, n=7) or UAS:*STMN1* (H, n=7) at one cell stage and fixed at 24 hpf.
962 Embryos were labelled with anti-GFP (green) and counterstained with Hoechst (blue). Note

963 that *STMNI* overexpression but not GFP prevents RPE cell flattening and cells retain a
964 cuboidal like shape (white arrowheads in G-H). The average invagination angle and mean
965 length of the A-B axis are indicated in the bottom left and right angles, respectively. **I, J**) The
966 graphs show the length of the A-B axis (I) and the invagination angle (J) in embryos
967 overexpressing GFP or *STMNI*. Mean \pm SD. ** $p < 0.01$). Scale bar: 50 μ m.

968

969 **Figure 5-figure supplement 2. Nocodazole treatment does not alter RPE specification**
970 **and polarity.** (A) DMSO and (B) Nocodazole-treated embryos (2.5 hr incubation from 17-
971 19.5 hpf, as reported in Fig. 5) hybridized with *otx1* specific probe. (C) DMSO or (D)
972 Nocodazole-treated embryos with *mitfa* specific probe. After Nocodazole treatment both
973 mRNA are specifically detected in the RPE (black arrowheads) despite its morphogenesis is
974 impaired. (E, E') Wild type embryos labelled with laminin (green/basal), *zo-1* (white/apical)
975 and Hoechst (blue) after DMSO or (F, F') nocodazole treatment. In both cases apico-basal
976 polarity is maintained (white and green arrowheads), even after depolymerizing microtubules
977 when RPE cells do not flatten correctly. A-D images are dorsal views of flat mounted
978 embryos. E-F' images are frontal sections of one eye. Scale bars: 100 μ m in A-D and 50 μ m
979 in E-F'

980

981 **Figure 6. Zebrafish RPE flattening is associated with an abrupt decrease of cell**
982 **proliferation.** (A) Confocal images of dorsally viewed Tg(E1-*bhlhe40*:GFP) embryos
983 exposed to BrdU at different developmental stages as indicated in the panel and
984 immunostained for BrdU (magenta) and GFP (green). **B**) Percentage of RPE proliferating
985 cells (BrdU+/total Hoechst +) in 17-48 hpf Tg(E1-*bhlhe40*:GFP) embryos. Mean \pm SD; n=5
986 embryos per stage. Scale bar: 100 μ m.

987

988 **Figure 7-figure supplement 1. Proliferation accounts for RPE surface increase during**
989 **amniotes OV folding.** **A**) Confocal images of frontal sections from E9.5 and E10.5 mouse
990 embryos co-immunostained for the RPE specific marker OTX2 (green) and actin (red).
991 Sections were counterstained with Hoeschst (blue). **B**) Confocal images of horizontal sections
992 from human embryos at CS15 and P5. The embryonic sections were immunostained for
993 OTX2 (green) and N-cadherin (red) counterstained with Hoeschst (blue). Postnatal sections
994 were immunostained for OTX2 (red). The distribution of OTX2 was used to define the
995 prospective RPE region whereas actin/N-cadherin distribution to identify the apico-basal axis
996 of the cells. Scale bars: 100 μ m in A and left B panel; 30 μ m in B right panel.

997

998 **Figure 7. Proliferation accounts for RPE surface increase during amniotes OV folding.**

999 **A-C)** Confocal images of frontal sections from medaka, chick and mouse embryos exposed to
1000 BrdU at equivalent stages of OV folding into OC, as indicated in the panels. Sections were
1001 immunostained for BrdU (green) and counterstained with Hoeschst (blue). In all panels, the
1002 prospective RPE has been highlighted with dotted white lines on the basis of the Otx2
1003 immunostaining illustrated in Figure 7-figure supplement 1. **D)** Confocal images of
1004 horizontal sections from human embryos at equivalent stages of OV folding into OC. Sections
1005 were immunostained for Ki67 (green) and counterstained with Hoeschst (blue). **E)** Percentage
1006 of RPE proliferating cells (BrdU+/total Hoechst+) in the analysed period and compared to
1007 those reported in Fig. 6B for zebrafish. Data represent mean \pm SD; the number of embryos
1008 analysed for each stage varied between 3 to 10. **F)** Relationship between proliferation rate and
1009 apico-basal axis length at OC stage in the different species. Note that there is a positive
1010 correlation between the two parameters. Scale bars: 50 μ m in A and 100 μ m in B-D.

1011

1012 **Figure 8. Summary of species-specific modes of RPE differentiation and its contribution**

1013 **to OV folding.** **A)** The drawing on the top represent the dynamic of OV folding into an OC.
1014 Green double arrow indicated RPE flattening, blue arrow rim involution whereas pink arrows
1015 indicate retinal basal constriction. Bottom row summarize the alterations in OV folding
1016 observed after localized interference with RPE and NR cytoskeleton. **B)** Schematic
1017 representation of the differential mechanisms by which the RPE in zebrafish (upper row) and
1018 in amniotes (lower row) expands its surface during OV folding morphogenesis. In zebrafish,
1019 the RPE enlarges its surface by cell stretching; in amniotes, including in humans, the RPE
1020 instead expands by cell proliferation with a less pronounced need of cell flattening.

1021 **Video Legends**

1022 **Video 1:** Dorsal view of the OV to OC transition visualized in a double Tg(E1-*bhlhe40*:GFP;
1023 *rx3*:GAL4;UAS:RFP embryo. Single confocal section, related to Fig. 1, frame rate 1/5min.

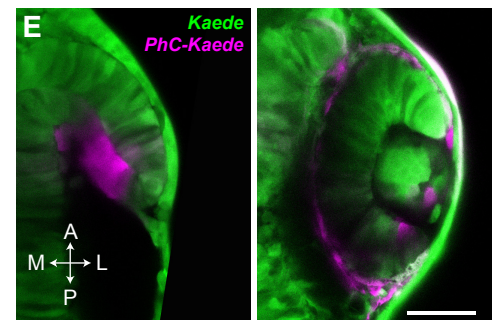
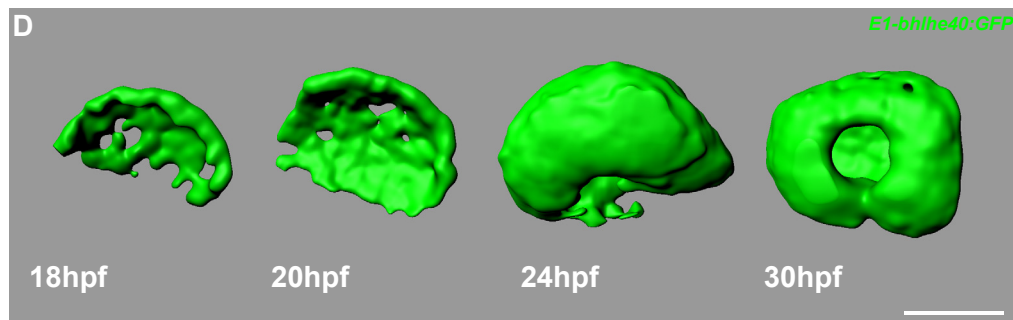
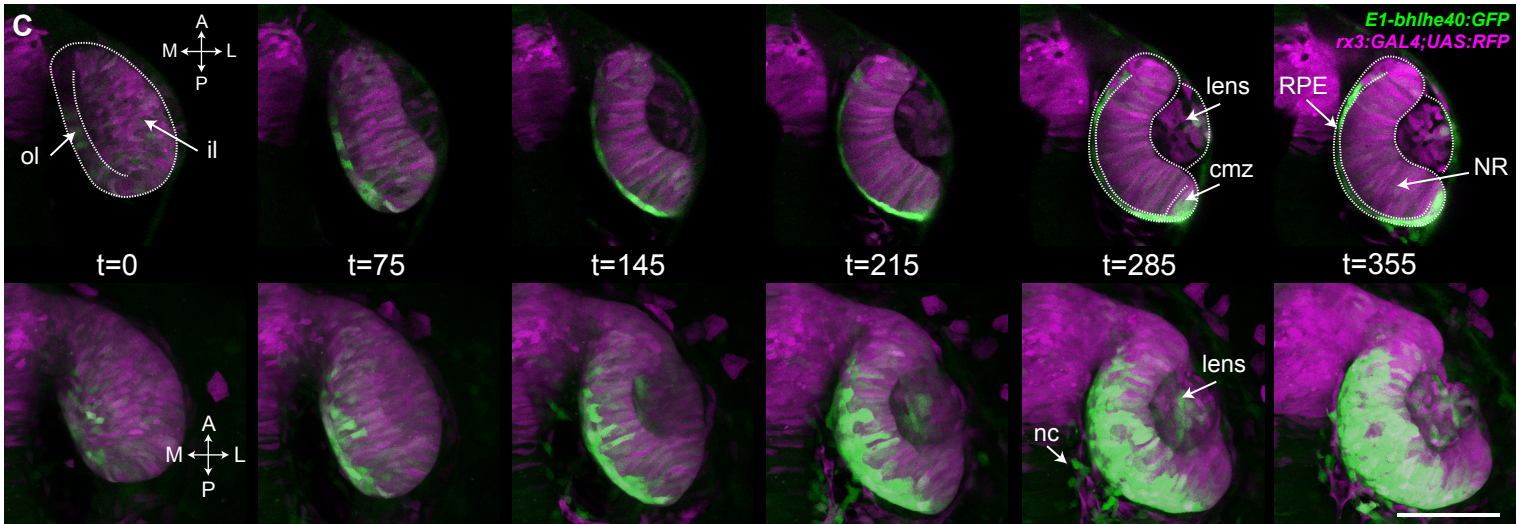
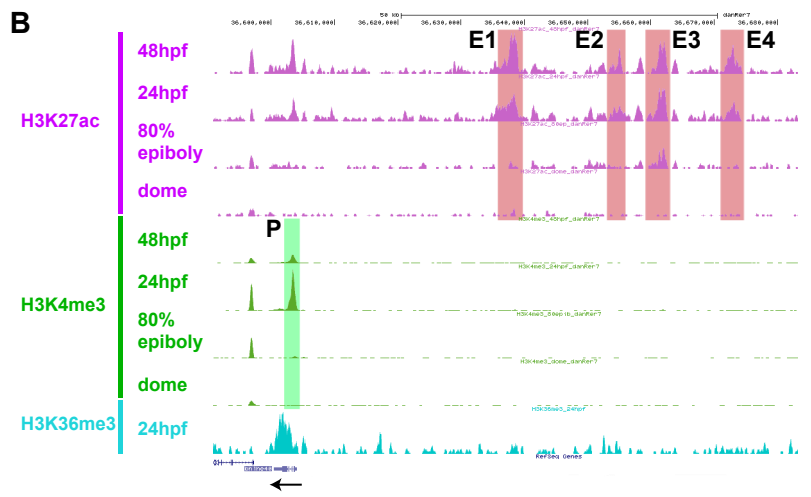
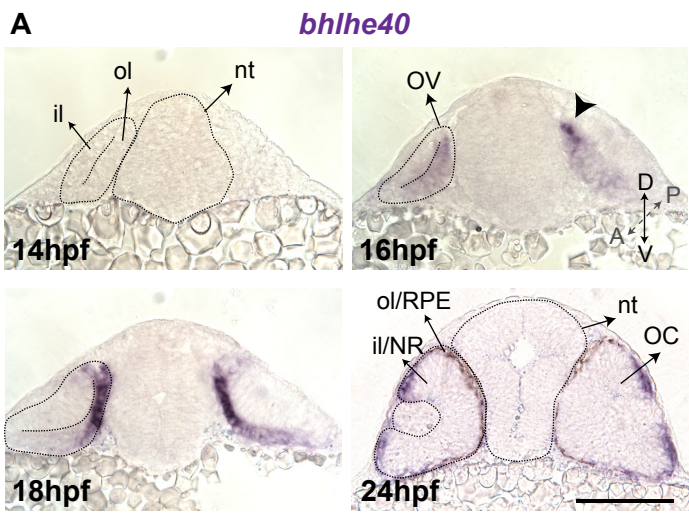
1024 **Video 2:** Dorsal view of the OV to OC transition visualized in a double Tg(E1-*bhlhe40*:GFP;
1025 *rx3*:GAL4;UAS:RFP embryo. Maximum projection reconstruction, related to Fig. 1, frame
1026 rate 1/5min.

1027 **Video 3:** Lateral view of the OC folding visualized in a Tg(E1-*bhlhe40*:GFP) embryo injected
1028 with H2B-RFP mRNA (magenta) related to Fig. 1, frame rate 1/5min.

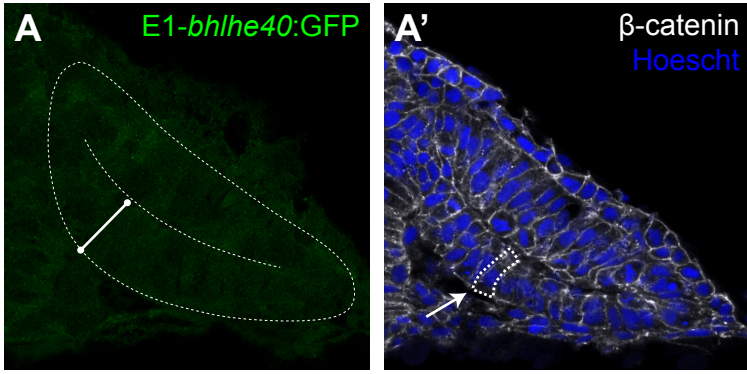
1029 **Video 4:** Lateral view of OC growth visualized in a Tg(E1-*bhlhe40*:GFP) embryo injected
1030 with H2B-RFP mRNA (magenta), related to Fig. 3, frame rate 1/5min)

1031 **Video 5:** *eb3*GFP dynamics 14, 17 and 23 hpf, when RPE cells have a neuroepithelial
1032 (continuous acquisition, n = 9), cuboidal (continuous acquisition, n = 10) or squamous
1033 conformation (continuous acquisition, n = 9).

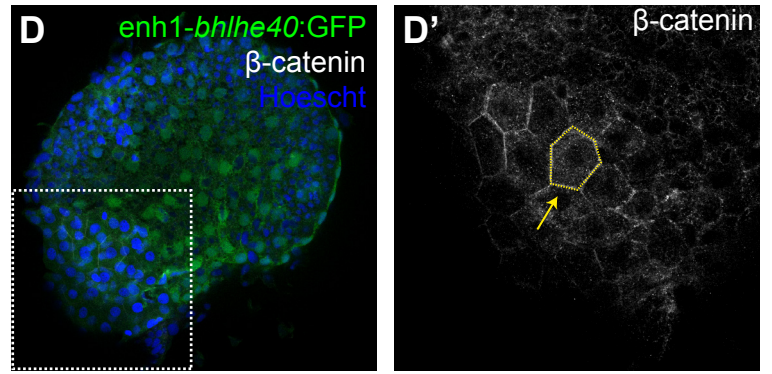
1034



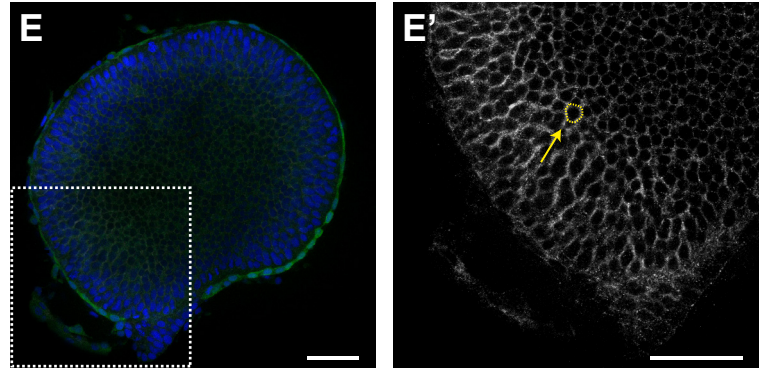
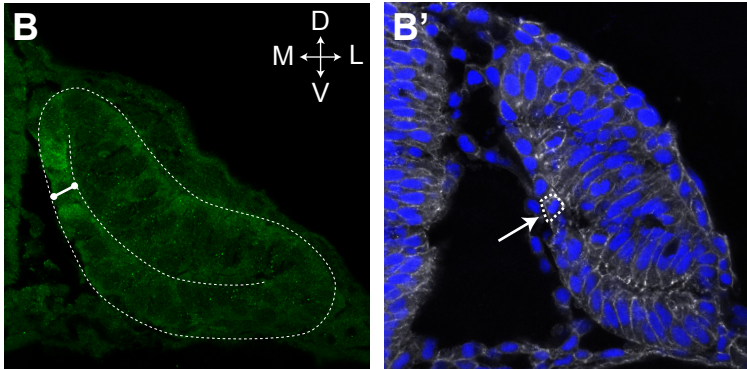
Pseudostratified epithelium



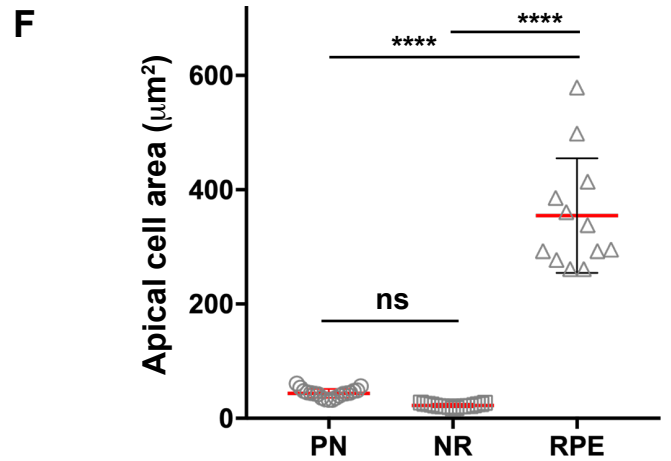
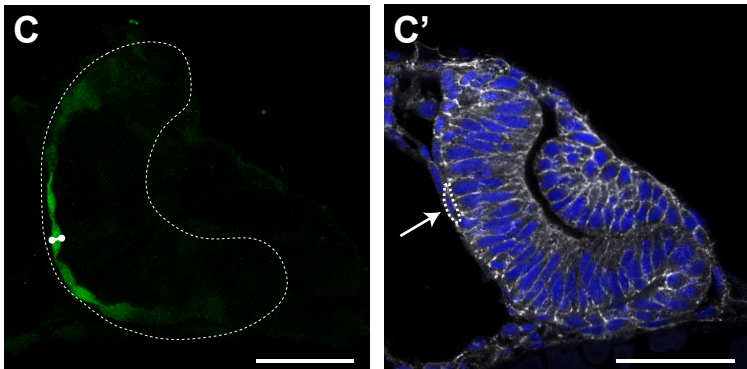
Medial cell area

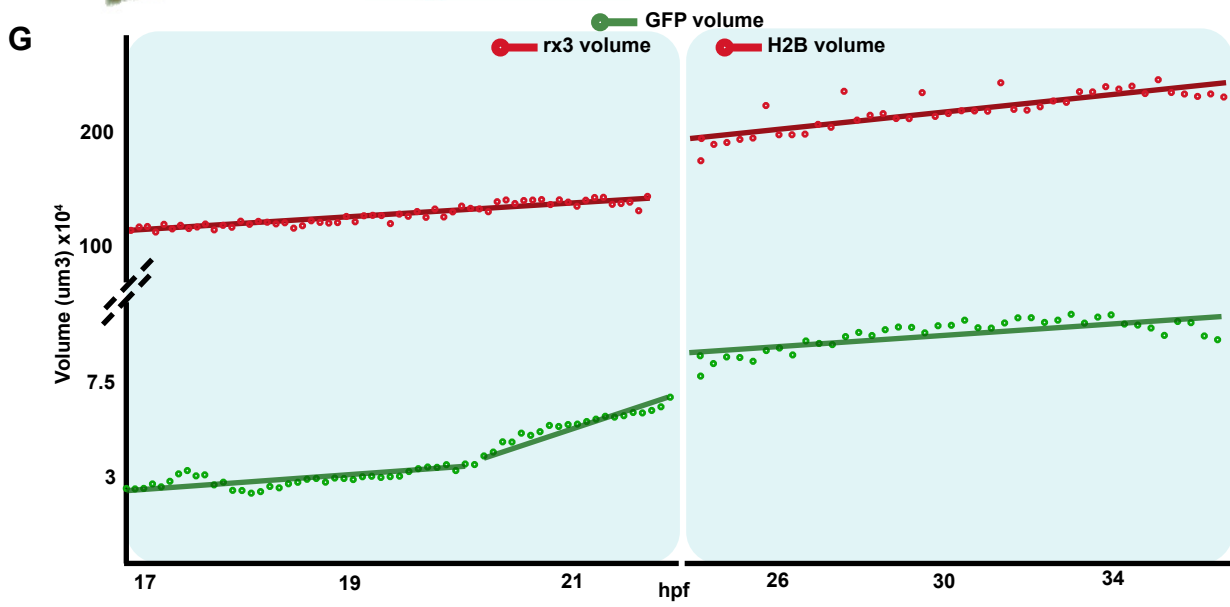
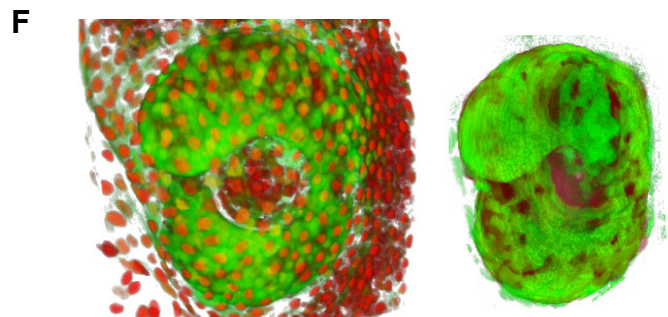
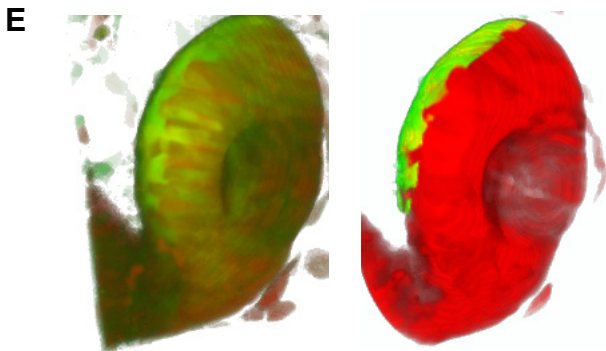
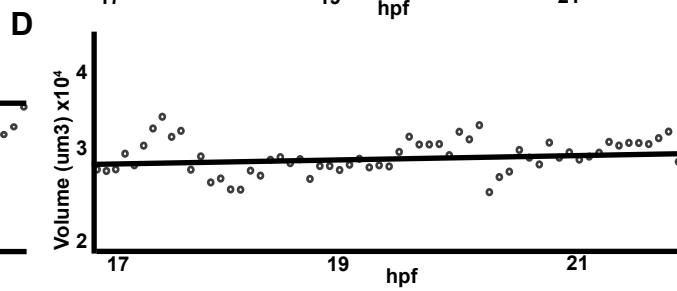
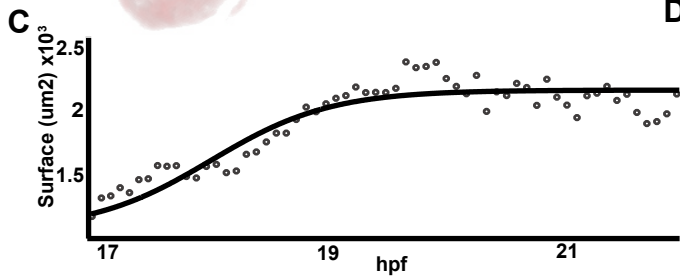
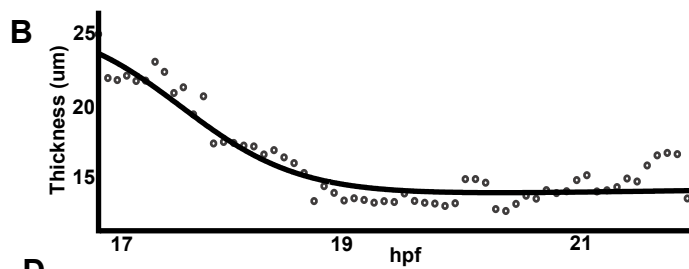
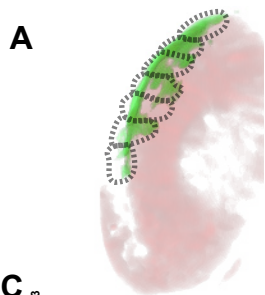


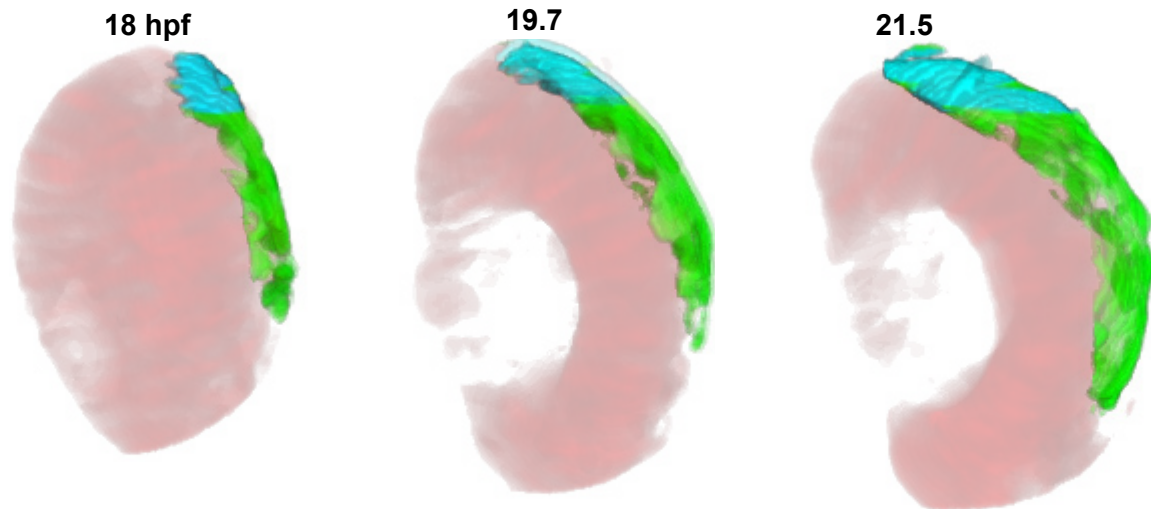
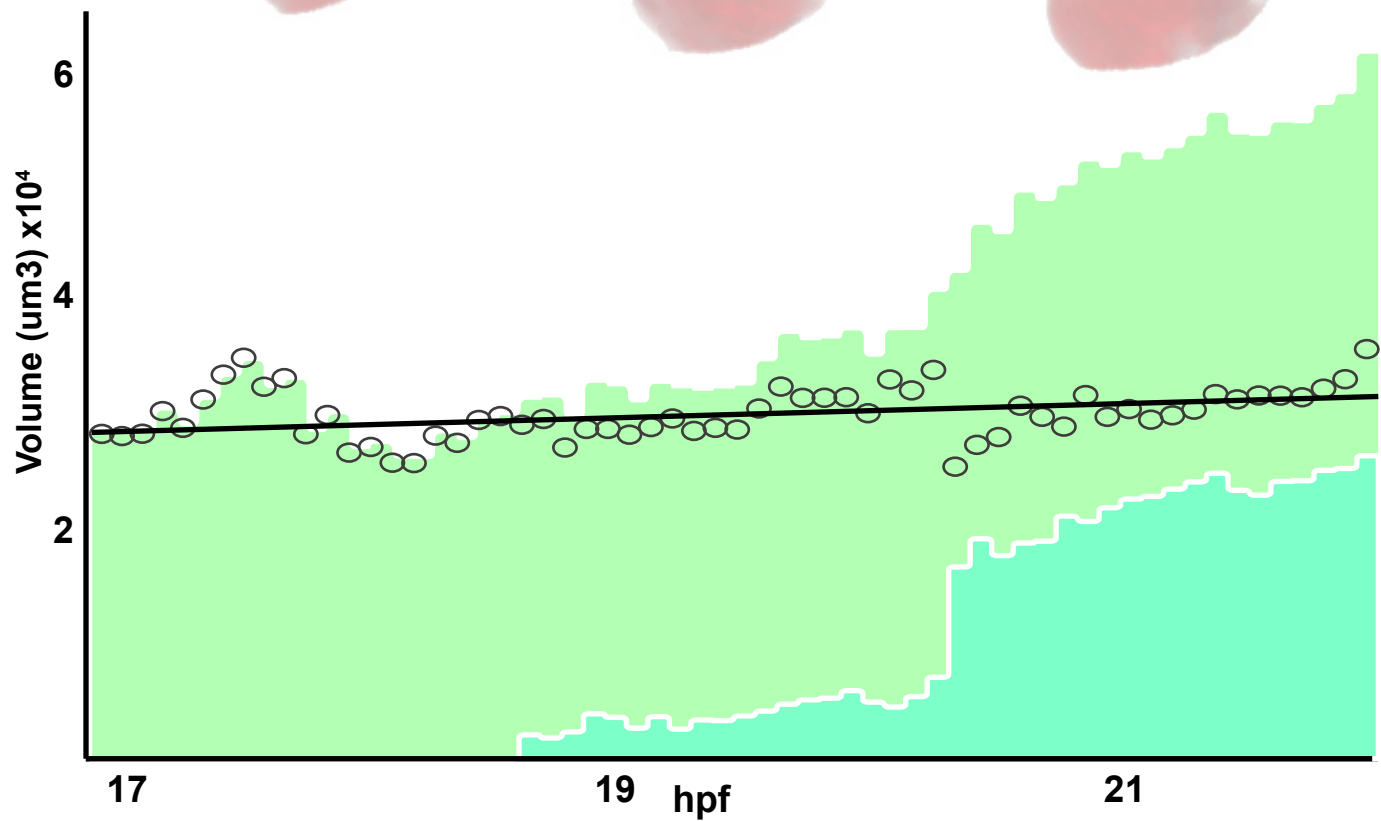
Cuboidal epithelium

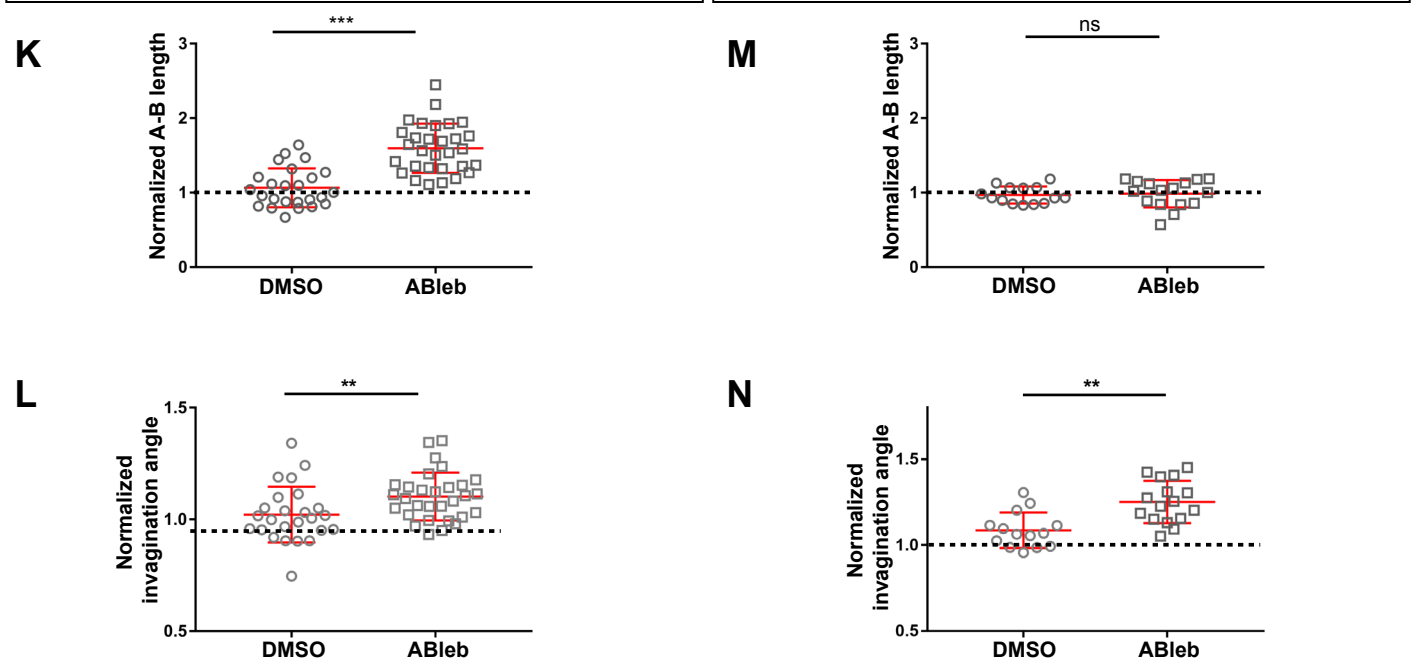
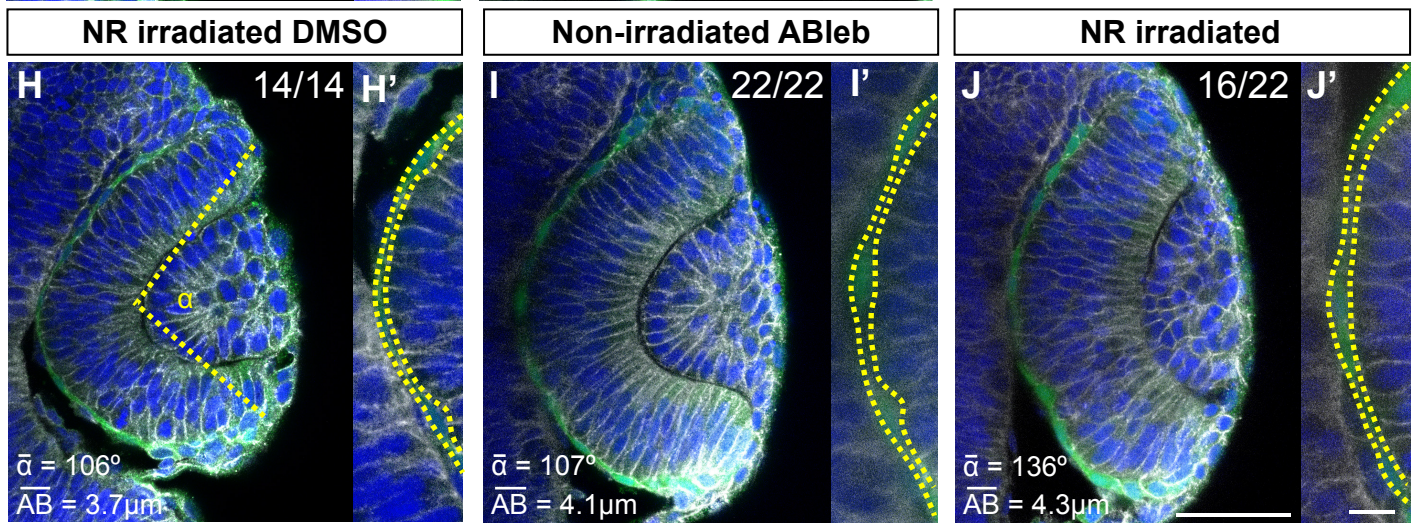
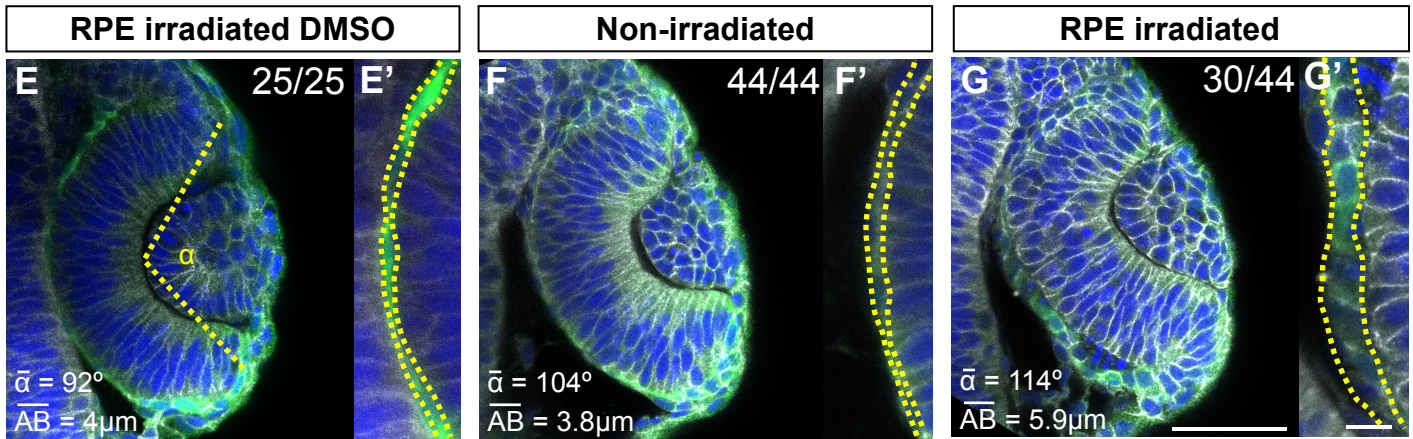
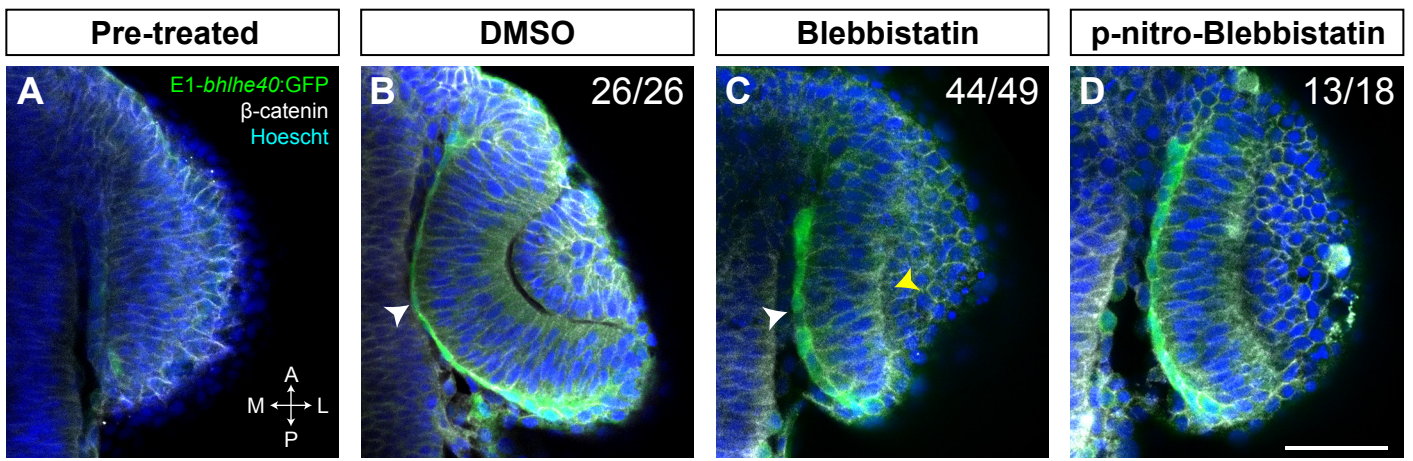


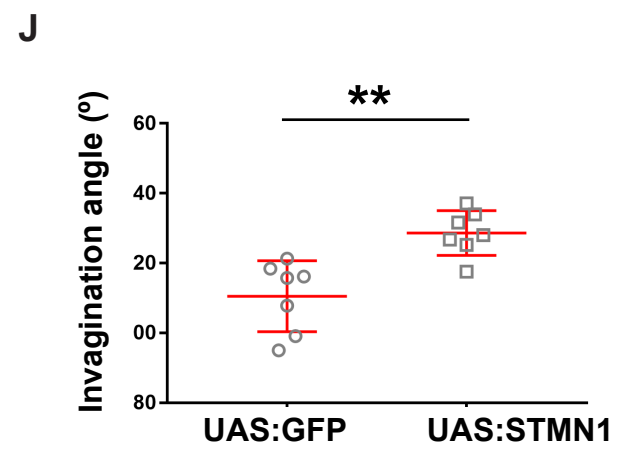
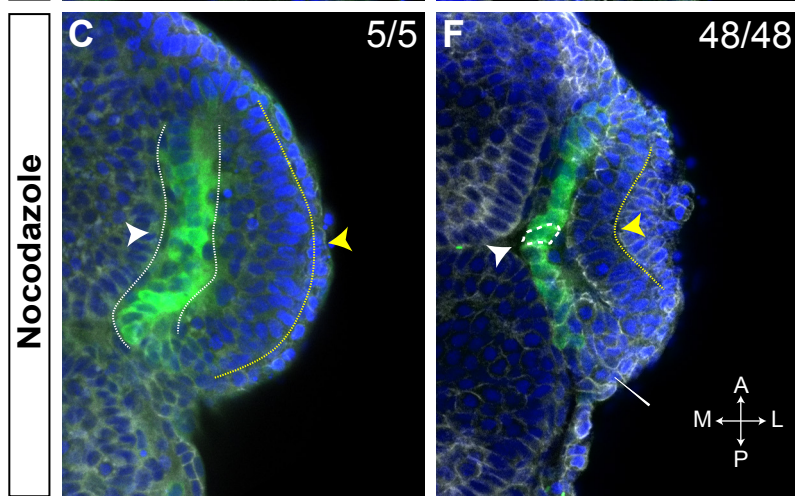
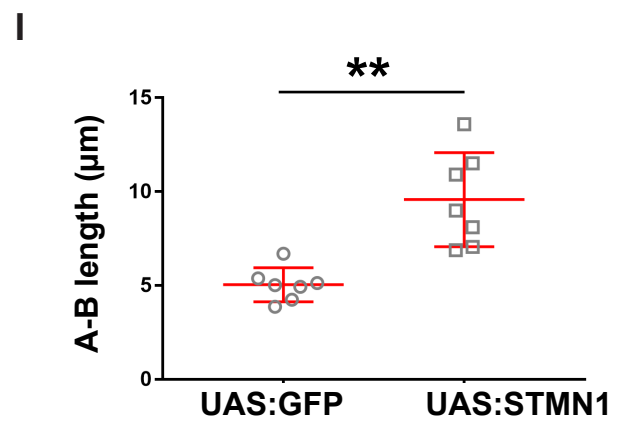
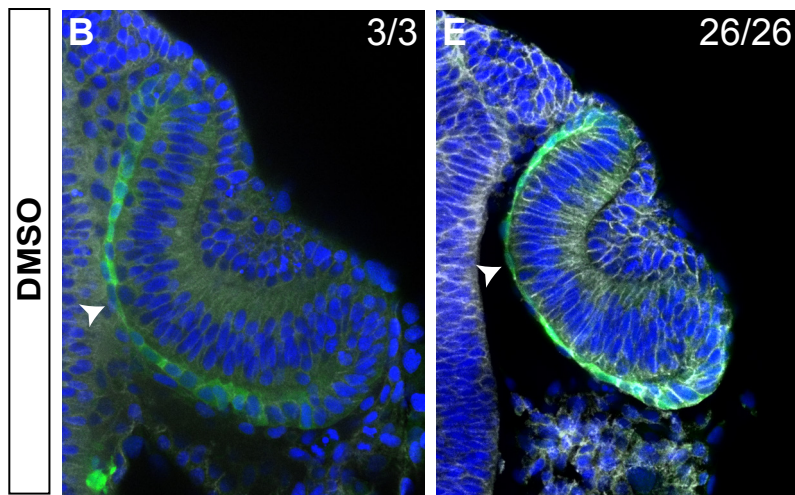
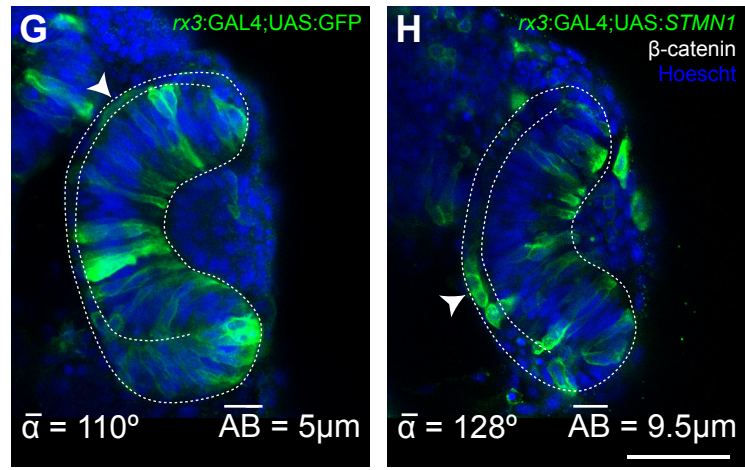
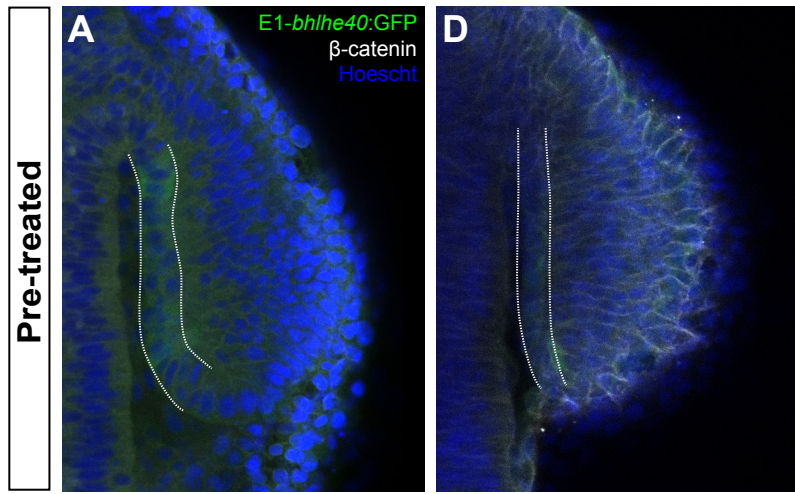
Flat epithelium

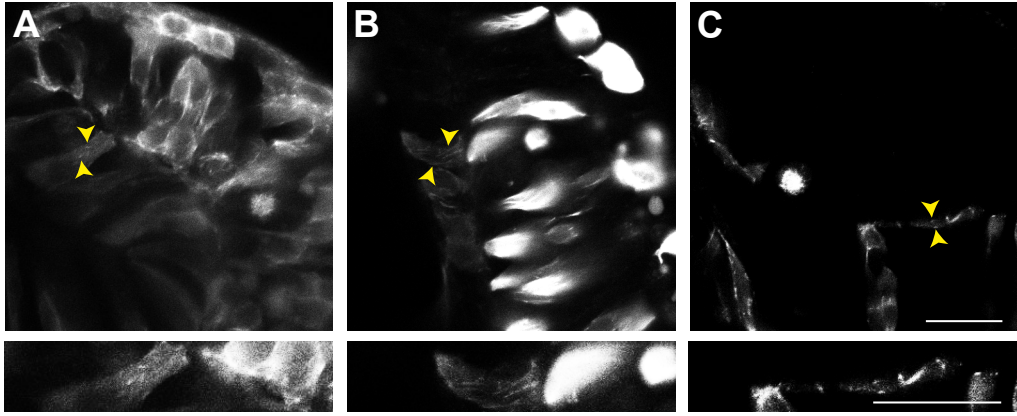




A**B**







25um

